The Astrophysical Journal, 946:66 (15pp), 2023 April 1 https://doi.org/10.3847/1538-4357/acb694

Phase-space Properties and Chemistry of the Sagittarius Stellar Stream Down to the Extremely Metal-poor ([Fe/H] $\lesssim -3$) Regime

Guilherme Limberg[1,2,3], Anna B. A. Queiroz[4,5], Hélio D. Perottoni[1,6], Silvia Rossi[1], João A. S. Amarante[6,7,14], Rafael M. Santucci[8,9], Cristina Chiappini[4,10], Angeles Pérez-Villegas[11], and Young Sun Lee[12,13]
[1] Universidade de São Paulo, Instituto de Astronomia, Geofísica e Ciências Atmosféricas, Departamento de Astronomia, SP 05508-090, São Paulo, Brasil; guilherme.limberg@usp.br
[2] Department of Astronomy & Astrophysics, University of Chicago, 5640 S. Ellis Avenue, Chicago, IL 60637, USA
[3] Kavli Institute for Cosmological Physics, University of Chicago, Chicago, IL 60637, USA
[4] Leibniz-Institut für Astrophysik Potsdam (AIP), An der Sternwarte 16, D-14482 Potsdam, Germany
[5] Institut für Physik und Astronomie, Universität Potsdam, Haus 28 Karl-Liebknecht-Strasse 24/25, D-14476 Golm, Germany
[6] Institut de Ciències del Cosmos (ICCUB), Universitat de Barcelona (IEEC-UB), Martí i Franquès 1, E-08028 Barcelona, Spain
[7] Jeremiah Horrocks Institute, University of Central Lancashire, Preston, PR1 2HE, UK
[8] Universidade Federal de Goiás, Instituto de Estudos Socioambientais, Planetário, Goiânia, GO 74055-140, Brasil
[9] Universidade Federal de Goiás, Campus Samambaia, Instituto de Física, Goiânia, GO 74001-970, Brasil
[10] Laboratório Interinstitucional de e-Astronomia—LIneA, RJ 20921-400, Rio de Janeiro, Brasil
[11] Instituto de Astronomía, Universidad Nacional Autónoma de México, Apartado Postal 106, C.P. 22800, Ensenada, B.C., Mexico
[12] Department of Astronomy and Space Science, Chungnam National University, Daejeon 34134, Republic of Korea
[13] Department of Physics and Astronomy and JINA Center for the Evolution of the Elements, University of Notre Dame, Notre Dame, IN 46556, USA
Received 2022 December 15; revised 2023 January 20; accepted 2023 January 24; published 2023 March 30

Abstract

In this work, we study the phase-space and chemical properties of the Sagittarius (Sgr) stream, the tidal tails produced by the ongoing destruction of the Sgr dwarf spheroidal (dSph) galaxy, focusing on its very metal-poor (VMP; [Fe/H] < -2) content. We combine spectroscopic and astrometric information from SEGUE and Gaia EDR3, respectively, with data products from a new large-scale run of the `StarHorse` spectrophotometric code. Our selection criteria yield ∼1600 stream members, including >200 VMP stars. We find the leading arm ($b > 0°$) of the Sgr stream to be more metal-poor, by ∼0.2 dex, than the trailing one ($b < 0°$). With a subsample of turnoff and subgiant stars, we estimate this substructure's stellar population to be ∼1 Gyr older than the thick disk's. With the aid of an *N*-body model of the Sgr system, we verify that simulated particles stripped earlier (>2 Gyr ago) have present-day phase-space properties similar to lower metallicity stream stars. Conversely, those stripped more recently (<2 Gyr) are preferentially akin to metal-rich ([Fe/H] > -1) members of the stream. Such correlation between kinematics and chemistry can be explained by the existence of a dynamically hotter, less centrally concentrated, and more metal-poor population in Sgr dSph prior to its disruption, implying that this galaxy was able to develop a metallicity gradient before its accretion. Finally, we identified several carbon-enhanced metal-poor ([C/Fe] $> +0.7$ and [Fe/H] $\leqslant -1.5$) stars in the Sgr stream, which might be in tension with current observations of its remaining core where such objects are not found.

Unified Astronomy Thesaurus concepts: Stellar streams (2166); Dwarf galaxies (416); CEMP stars (2105); Galactic archaeology (2178); Milky Way stellar halo (1060); Stellar kinematics (1608)

1. Introduction

The Galactic stellar halo is expected to be assembled through a succession of merging events between the Milky Way and dwarf galaxies of various masses in the context of the hierarchical formation paradigm (Searle & Zinn 1978; White & Frenk 1991; Kauffmann et al. 1993; Springel et al. 2006). Upon interacting with the Galactic gravitational potential well, the constituent stars of these satellites become tidally unbound, and over time, phase mixed into a smooth halo (e.g., Helmi & White 1999). The intermediate stage of this process is characterized by the appearance of stellar streams, spatially elongated structures produced by accreted debris that remains kinematically cohesive (Johnston 1998; Bullock & Johnston 2005; Cooper et al. 2010, 2013; Pillepich et al. 2015; Morinaga et al. 2019).

The magnificence of immense stellar streams can be appreciated both in external massive galaxies (e.g., M31/Andromeda, NGC 5128/Centaurus A, and M104/Sombrero; Ibata et al. 2001a; Crnojevic et al. 2016; Martinez-Delgado et al. 2021) as well as in the Milky Way itself (e.g., Belokurov et al. 2006). The archetype of the above-described process is the Sagittarius (Sgr) stream (e.g., Mateo et al. 1998), the tidal tails produced by the destruction of the Sgr dwarf spheroidal (dSph) galaxy (Ibata et al. 1994, 1995).

Over the past couple of decades, the Sgr stream has been mapped across ever-increasing areas of the sky (Alard 1996; Mateo, et al. 1996; Mateo et al. 1998; Ibata et al. 2001b; Newberg et al. 2003; Martinez-Delgado et al. 2004). Eventually, wide-area photometric data allowed us to contemplate the grandiosity of the Sgr stream throughout both hemispheres (Majewski et al. 2003; Yanny et al. 2009a). Furthermore, observations of distant halo tracers (e.g., RR Lyrae stars; Vivas et al. 2005) and line-of-sight velocity (v_{los}) measurements (Majewski et al. 2004) served as constraints for

[14] Visiting Fellow at UCLan.

an early generation of *N*-body simulations that attempted to reproduce the phase-space properties of the stream (Helmi & White 2001; Helmi 2004; Johnston et al. 2005; Law et al. 2005; Fellhauer et al. 2006; Penarrubia et al. 2010). These works culminated in the landmark model of Law & Majewski (2010), which was capable of reproducing most of the Sgr stream's features known at the time.

Thanks to the Gaia mission (Gaia Collaboration et al. 2016a, 2016b, 2018, 2021), precise astrometric data for more than a billion stars in the Milky Way are now available, revolutionizing our views of the Milky Way and the knowledge about Galactic stellar streams (e.g., Malhan et al. 2018; Price-Whelan & Bonaca 2018; Shipp et al. 2019; Riley & Strigari 2020; Li et al. 2021). For instance, it has allowed the blind detection of $\mathcal{O}(10^5)$ high-probability members of the Sgr stream (Antoja et al. 2020; Ibata et al. 2020; Ramos et al. 2022), dramatically advancing our understanding of its present-day kinematics. Moreover, a misalignment between the stream's track and the motion of its debris has been identified toward the leading arm (Galactic latitude $b > 0°$) of Sgr (Vasiliev et al. 2021, hereafter V21). Such observation can be reconciled with time-dependent perturbations induced by the Large Magellanic Cloud (LMC; see Oria et al. 2022 and Wang et al. 2022).

Despite these Gaia-led advances, a fundamental difficulty in studies of the Sgr stream continues to be the large heliocentric distances of its member stars ($\gtrsim$10 kpc as informed by, e.g., the aforementioned V21 model). This challenge is usually tackled via the utilization of stellar standard candles appropriate for the study of old stellar populations such as blue horizontal-branch and RR Lyrae stars (e.g., Belokurov et al. 2014; Hernitschek et al. 2017; Ramos et al. 2020), allowing us to identify the Sgr stream in angular-momentum space (Penarrubia & Petersen 2021, hereafter PP21) or in integrals of motion (Yang et al. 2019; Yuan et al. 2019, 2020a).

Although the usage of some specific halo tracers has been crucial for advancing our knowledge of the dynamical status of the Sgr stream, it comes with the obvious caveat of limited sample sizes. One way to go about this is to leverage both spectroscopic and photometric information from large-scale surveys in order to obtain full spectrophotometric distance estimates (Santiago et al. 2016; Coronado et al. 2018; McMillan et al. 2018; Queiroz et al. 2018; Hogg et al. 2019; Leung & Bovy 2019) for much larger stellar samples.

Recently, Hayes et al. (2020) used spectrophotometric distances for stars observed during the Apache Point Observatory Galactic Evolution Experiment (APOGEE; Majewski et al. 2017) to investigate abundances in the Sgr system (stream+remnant). Significant chemical differences between the leading and trailing ($b < 0°$) arms were reported, with the latter being more metal-rich (by $\sim$0.3 dex) than the former (see also Monaco et al. 2005, 2007; Li et al. 2016; Carlin et al. 2018; Li et al. 2019, and Ramos et al. 2022), as well as [Fe/H] and [α/Fe] gradients *along* the stream itself (e.g., Bellazzini et al. 2006; Chou et al. 2007, 2010; Keller et al. 2010; Shi et al. 2012, and Hyde et al. 2015). Moreover, Johnson et al. (2020, hereafter J20) investigated the stellar population(s) of the Sgr stream with data from the Hectochelle in the Halo at High Resolution (H3; Conroy et al. 2019) survey and spectrophotometric distances derived as in (Cargile et al. 2020, see also Naidu et al. 2020). The extended metallicity range (reaching [Fe/H] ≈ -3) probed by H3, in comparison to APOGEE ([Fe/H] $\gtrsim -2$; see Limberg et al. 2022 for a discussion), allowed these authors to uncover a metal-poor, dynamically hot, and spatially diffuse component of the Sgr stream, confirming a suggestion by Gibbons et al. (2017).

In this contribution, we explore the phase-space and chemical properties of the Sgr stream, but focus on its very metal-poor (VMP; [Fe/H] < -2)[15] population, seeking to quantify the whole evolution of its kinematics as a function of chemistry. For this task, we need a large enough sample of stars covering a wide metallicity range. Therefore, our attention was drawn to low-resolution ($\mathcal{R} \sim 1800$) spectroscopic data from the Sloan Extension for Galactic Understanding and Exploration (SEGUE; Yanny et al. 2009b; Rockosi et al. 2022) survey, a subproject within the Sloan Digital Sky Survey (SDSS; York et al. 2000). Atmospheric parameters provided by the SEGUE Stellar Parameter Pipeline (SSPP; Lee et al. 2008a, 2008b; Allende Prieto et al. 2008; Lee et al. 2011; Smolinski et al. 2011) are combined with Gaia's parallaxes and broadband photometry from various sources, similar to those in Queiroz et al. (2020), to estimate spectrophotometric distances for $\sim$175,000 low-metallicity ($-3.5 \lesssim$ [Fe/H] $\leqslant -0.5$) stars in the SEGUE catalog. The complete description of this effort, including other spectroscopic surveys, is reserved for an accompanying paper (Queiroz et al. 2023).

This work is organized as follows. Section 2 describes the observational data analyzed throughout this work. Section 3 is dedicated to investigating the chemodynamical properties of the Sgr stream in SEGUE. Comparisons with the *N*-body model of V21 are presented in Section 4. We explore α-element and carbon abundances in Section 5. Finally, Section 6 is reserved for a brief discussion and our concluding remarks.

2. Data

2.1. SEGUE+Gaia and `StarHorse`

SEGUE's emphasis on the distant halo is suitable for studying Sgr (and other streams; Koposov et al. 2010; Newberg et al. 2010) and has, indeed, been extensively explored for this purpose (Yanny et al. 2009a; Belokurov et al. 2014; de Boer et al. 2014, 2015; Gibbons et al. 2017; Chandra et al. 2022; Thomas & Battaglia 2022). The novelty is the availability of complete phase-space information thanks to Gaia. Hence, we are in a position to construct a larger sample of confident Sgr stream members than previous efforts.

Stellar atmospheric parameters, namely, effective temperatures ($T_{\rm eff}$), surface gravity ($\log g$), and metallicities (in the form of [Fe/H]), as well as α-element abundances ([α/Fe]), and $v_{\rm los}$ values for SEGUE stars were obtained via application of the SSPP[16] routines. The final run of the SSPP to SEGUE spectra was presented alongside the ninth data release (DR9) of SDSS (Ahn et al. 2012) and has been included, unchanged, in all subsequent DRs. Recently, Rockosi et al. (2022) reevaluated the internal precision of SSPP's atmospheric parameters for DR9, which are no worse than 80 K, 0.35 dex, and 0.25 dex for $T_{\rm eff}$, $\log g$, and [Fe/H], respectively, across the entire metallicity and color ranges explored. Unless explicitly stated, we consider SEGUE's as our fiducial stellar parameters throughout the remainder of this paper. These also serve as

[15] Following the convention of Beers & Christlieb (2005).

[16] Over the years, the SSPP has also been expanded to deliver carbon (Carollo et al. 2012; Lee et al. 2013, 2017, 2019; Arentsen et al. 2022), nitrogen (Kim et al. 2022), and sodium (Koo et al. 2022) abundances (see Section 5.2).

input for the Bayesian isochrone-fitting code StarHorse (Santiago et al. 2016; Queiroz et al. 2018), which, in turn, provides ages and distances.

In this work, we only consider spectra with moderate signal-to-noise ratio ($S/N > 20$ pixel^{-1}). We keep only those stars within $4500 < T_{\rm eff}/K < 6500$, which is the optimal interval for the performance of SSPP. Moreover, we limit our sample to low-metallicity stars ($[Fe/H] \leqslant -0.5$), which removes most of the contamination from the thin disk, but maintains the majority of Sgr stream members; out of 166 stars analyzed by Hayes et al. (2020), only five (3%) show $[Fe/H] > -0.5$.

We crossmatch the above-described SEGUE low-metallicity sample with Gaia's early DR3 (EDR3; Gaia Collaboration et al. 2021) using a 1.″5 search radius. In order to ensure the good quality of the data at hand, we only retain those stars whose renormalized unit weight errors are within the recommended range (ruwe $\leqslant 1.4$; Lindegren et al. 2021a). Parallax biases and error inflation are handled following Lindegren et al. (2021b) and Fabricius et al. (2021), taking into account magnitudes, colors, and on-sky positions. Stars with largely negative parallax values (parallax < -5 mas) are discarded. Also, we emphasize that only those stars with an available parallax measurement are considered to ensure good distance results. Those stars with potentially spurious astrometric solutions are also removed (fidelity_v2 < 0.5; Rybizki et al. 2022).

We applied StarHorse to this SEGUE+Gaia EDR3 sample in order to estimate precise distances that would allow us to study the Sgr stream. At $\geqslant$10 kpc from the Sun, our derived uncertainties are at the level of $\sim$13%. The medians of the derived posterior distributions are adopted as our nominal values, while 16th and 84th percentiles are taken as uncertainties. Further details regarding stellar-evolution models and geometric priors can be found in Queiroz et al. (2018, 2020) and Anders et al. (2019). See also Anders et al. (2022) for details regarding the compiled photometric data.

With the StarHorse output at hand, we restrict our sample to stars with moderate (<20%) fractional Gaussian uncertainties in their estimated distance values. We refer to this catalog as the "SEGUE/StarHorse low-metallicity sample" or close variations of that. We refer the interested reader to Perottoni et al. (2022) for an initial application of these data. Its coverage in a Cartesian Galactocentric projection can be appreciated in Figure 1. By color coding this plot with the mean [Fe/H] in spatial bins, the footprint of the Sgr stream is already perceptible as metal-rich trails at $|Z| \gtrsim 20$ kpc.

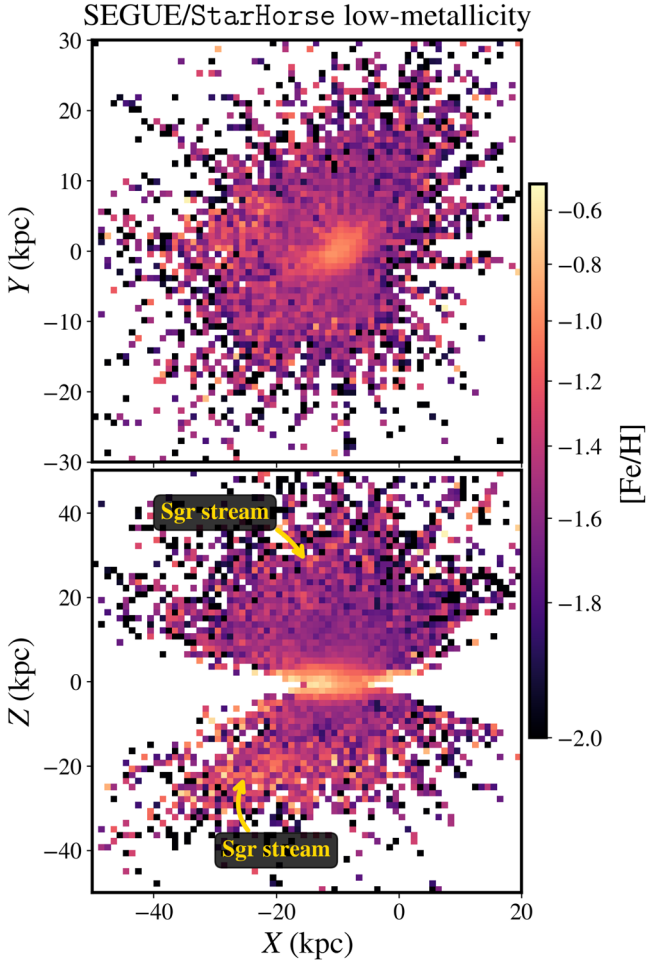

Figure 1. Cartesian Galactocentric projections of the SEGUE/StarHorse low-metallicity sample. Top: (X, Y). Bottom: (X, Z). Spatial bins are color coded by their mean [Fe/H] values. The attentive reader may notice the footprint of the Sgr stream as metal-rich trails at $|Z| \gtrsim 20$ kpc.

2.2. Kinematics and Dynamics

Positions (α, δ) and proper motions ($\mu_\alpha^* = \mu_\alpha \cos\delta$, μ_δ) on the sky, $v_{\rm los}$ values from SEGUE, and StarHorse heliocentric distances are converted to Galactocentric Cartesian phase-space coordinates using Astropy Python tools (Astropy Collaboration et al. 2013, 2018). The adopted position of the Sun with respect to the Galactic Center is (X, Y, Z)$_\odot$ = (−8.2, 0.0, 0.0) kpc (Bland-Hawthorn & Gerhard 2016; Bennett & Bovy 2019). The local circular velocity is $\boldsymbol{V}_{\rm circ}$ = (0.0, 232.8, 0.0) km s^{-1} (McMillan 2017), while the Sun's peculiar motion with respect to $\boldsymbol{V}_{\rm circ}$ is (U, V, W)$_\odot$ = (11.10, 12.24, 7.25) km s^{-1} (Schonrich et al. 2010).

For reference, we write, below, how each component of the total angular momentum ($\boldsymbol{L}$) is calculated.

$$\begin{aligned} L_x &= YV_z - ZV_y \\ L_y &= ZV_x - XV_z \\ L_z &= XV_y - YV_x, \end{aligned} \tag{1}$$

where $L = \sqrt{L_x^2 + L_y^2 + L_z^2}$. We recall that, although $\boldsymbol{L}$ is not fully conserved in an axisymmetric potential, with the exception of the L_z component, it has been historically used for the identification of substructure in the Galaxy as it preserves a reasonable amount of clumping over time (see Helmi 2020 for a review).

For the entire SEGUE/StarHorse low-metallicity sample, we also compute other dynamical parameters, such as orbital energy (E) and actions ($\boldsymbol{J} = (J_R, J_\phi, J_z)$ in cylindrical frame). The azimuthal action is equivalent to the vertical component of angular momentum ($J_\phi \equiv L_z$) and we use these nomenclatures interchangeably. In order to obtain these quantities, orbits are integrated for 10 Gyr forward with the AGAMA package (Vasiliev 2019) within the axisymmetric Galactic model of McMillan (2017). A total of 100 initial conditions were generated for each star with a Monte Carlo approach, accounting for uncertainties in proper motions, $v_{\rm los}$, and

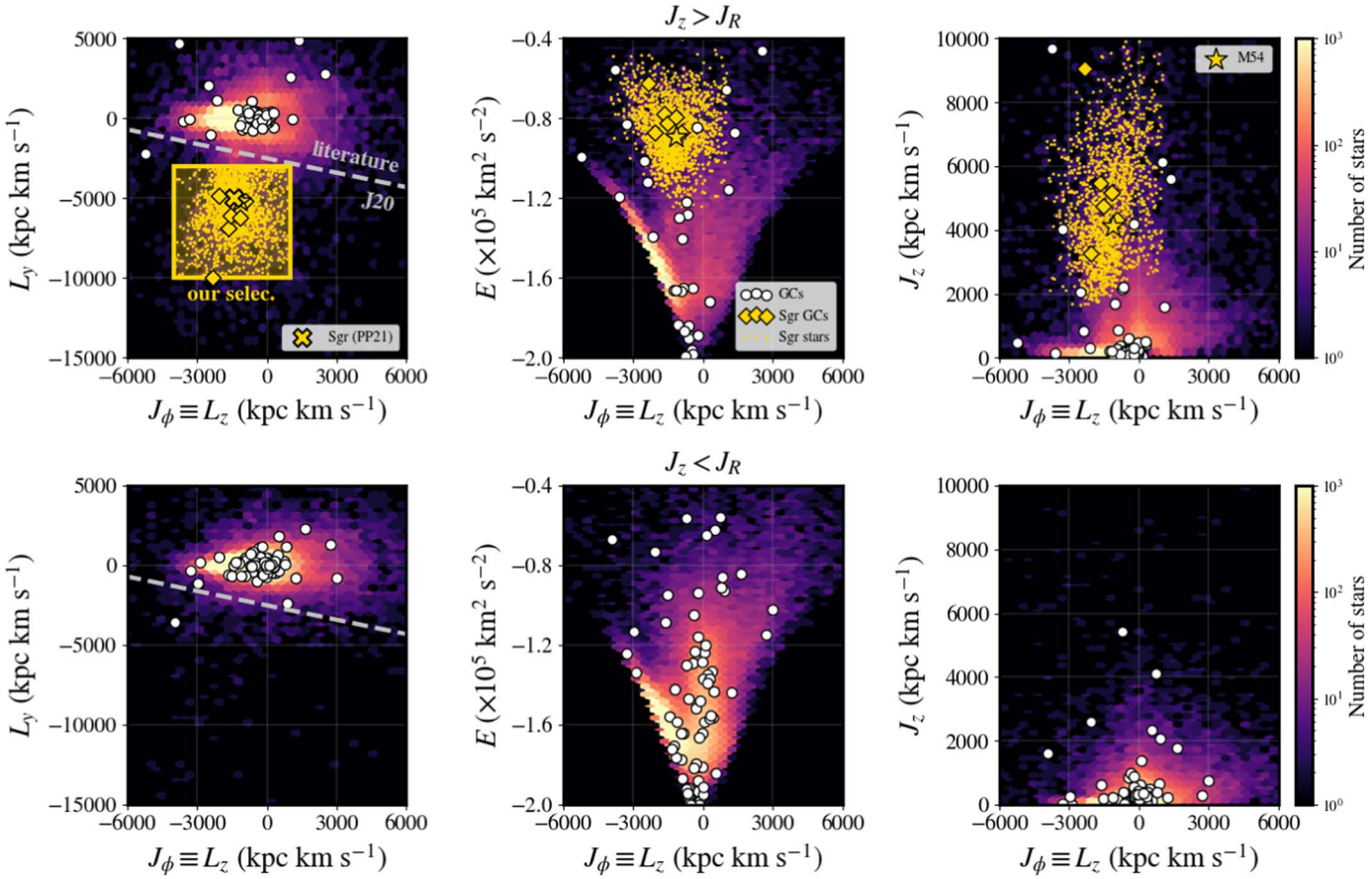

Figure 2. Upper row: $J_z > J_R$ (predominantly polar orbits). Bottom: $J_z < J_R$ (radial/eccentric orbits). Background density maps are produced with the full SEGUE/`StarHorse` low-metallicity sample. White dots are Galactic GCs. Those associated with the Sgr dSph/stream are displayed as yellow diamonds, with M54 denoted by the star symbol (see the text). Left panels: (L_z, L_y). Our Sgr stream selection is shown as the yellow box. The gray dashed line exhibits the J20 criterion. The yellow cross is the central location of Sgr in this space according to PP21. Yellow dots represent Sgr stream members. Middle: (L_z, E). Right: (L_z, J_z).

distance. The final orbital parameters are taken as the medians of the resulting distributions, with 16th and 84th percentiles as uncertainties.

3. Sgr Stream in SEGUE

3.1. Selection of Members

Given our goals, we seek to construct a sample of Sgr stream members that is both (i) larger in size and (ii) with greater purity than previously considered by J20, but (iii) with a similarly extended metallicity range, reaching the extremely metal-poor ([Fe/H] < -3) regime. J20 have shown that stars from the Sgr stream can be selected to exquisite completeness in the (L_z, L_y) plane, which exploits the polar nature of their orbits. We reproduce their criterion in Figure 2 (left panels, dashed lines). However, PP21 have recently argued that the J20's criterion also includes ≈21% of interlopers.

We inspect the aforementioned (L_z, L_y) plane, splitting it into $J_z > J_R$ (predominantly polar orbits; Figure 2, top row) and $J_z < J_R$ (radial/eccentric orbits; bottom row) as was done in Naidu et al. (2020). In Figure 2, there exists an excess of stars toward negative values of L_y (top left panel), which is prograde (top middle), and with $J_z \gtrsim 2000$ kpc km s^{-1} (top right; Thomas & Battaglia 2022), corresponding to the footprint of the Sgr stream (see Malhan et al. 2022). In the case where $J_z < J_R$, where the Sgr stream completely vanishes, the (L_z, E) space is dominated by the Gaia Sausage/Enceladus (GSE; Belokurov et al. 2018; Haywood et al. 2018, also Helmi et al. 2018).

Building on the above-described facts, we quantify how useful the $J_z > J_R$ condition is for eliminating potential GSE contaminants within our Sgr stream members. We look at a suite of chemodynamical simulations of Milky Way-mass galaxies with stellar halos produced by a single GSE-like merger presented in Amarante et al. (2022). Within these models, the fraction of GSE debris that end up (at redshift $z = 0$) on orbits with $J_z > J_R$ is always below 9%. Therefore, we incorporated this condition into our selection as it should remove >90% of potential GSE stars.

Lastly, we restrict the kinematic locus occupied by the Sgr stream in (L_z, L_y) in comparison to J20 and consider only those stars at >6 kpc from the Sun, in conformity with the V21 model. In this work, the conditions that a star must fulfill in order to be considered a genuine member of the Sgr stream are listed below:

1. $J_z > J_R$;
2. heliocentric distance > 6 kpc;
3. $-10 < L_y/(10^3 \text{ kpc km s}^{-1}) < -3$;
4. $-4 < L_z/(10^3 \text{ kpc km s}^{-1}) < +1$.

This selection is delineated by the yellow box in the top left panel of Figure 2. It is clear that our criteria are more conservative than J20's. Nevertheless, the raw size of our final Sgr stream sample (∼1600 stars) is twice as large as the one

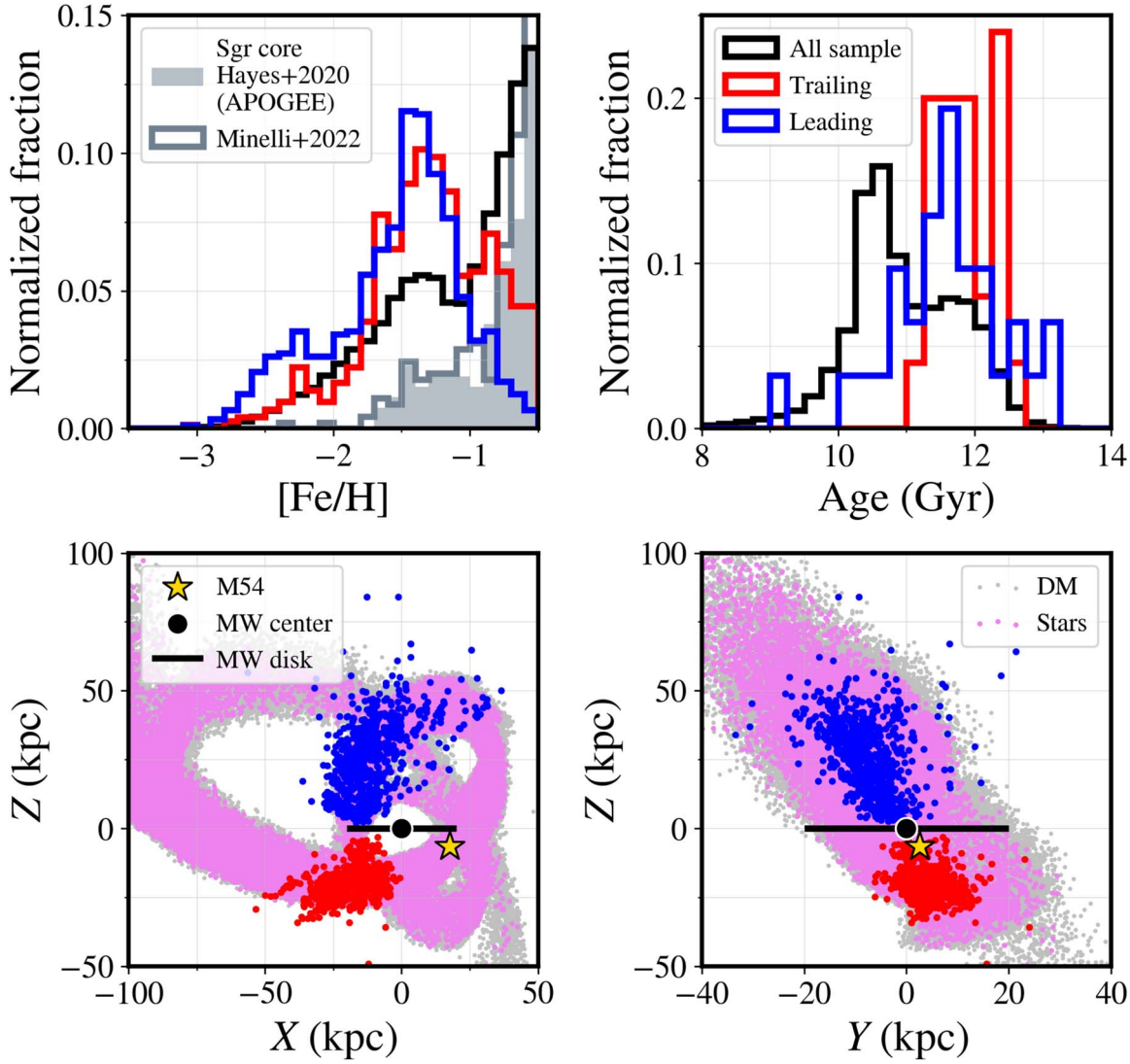

Figure 3. Top row: metallicity (left) and age (right) distributions. In both panels, blue and red histograms represent the leading and trailing arms of the Sgr stream, respectively. Filled and empty grayish histograms show the [Fe/H] distributions of Sgr's core according to Hayes et al. (2020, updated to APOGEE DR17) and Minelli et al. (2023), respectively. The complete SEGUE/`StarHorse` low-metallicity sample is shown in black. Bottom row: configuration space in the Galactic Cartesian coordinate system. Left: (*X*,*Z*). Right: (*Y*,*Z*). Blue and red dots represent stars associated with the leading and trailing arms, respectively. The location of the M54 GC, which coincides with the center of Sgr dSph, is shown as the yellow star symbol. The background Sgr model (stream+surviving core) is from V21, where gray and pink dots represent dark matter and stellar particles, respectively. The Milky Way's center and disk (40 kpc diameter) are illustrated by the black circle and line, respectively.

presented by these authors despite the sharp cut at [Fe/H] < -0.5. Moreover, the metallicity range covered reaches [Fe/H] ~ -3, with >200 VMP stars in the sample (top left in Figure 3). Finally, although these Sgr stream candidates were identified from their locus in (L_z, L_y), we found them to be spatially cohesive and in agreement with the V21 model in configuration space (bottom row of Figure 3). Even so, the potential contamination by other known polar streams (see Malhan et al. 2021) is explored in the Appendix.

With this new set of selection criteria at hand, we verified which known Galactic globular clusters (GCs) would be connected to the Sgr system. Consequently, we examined the orbital properties of 170 GCs from the Gaia EDR3-based catalog of Vasiliev & Baumgardt (2021). We found that a total of seven GCs can be linked to this group, including NGC 6715/M54, Whiting1, Koposov1, Terzan7, Arp2, Terzan8, and Pal12. We note that M54 has long been recognized to be the nuclear star cluster of Sgr dSph (e.g., Bellazzini et al. 2008). Furthermore, most of these other GCs had already been attributed to Sgr by several authors (Massari et al. 2019; Bellazzini et al. 2020; Forbes 2020; Kruijssen et al. 2020; Callingham et al. 2022; Malhan et al. 2022).

3.2. Leading and Trailing Arms

We begin our study of the Sgr stream's stellar populations by looking at the metallicity distributions obtained for the leading and trailing arms and the differences between them. In Figure 3, the immediately perceptible feature is the excess of VMP stars in the leading arm. On the contrary, the trailing arm presents a significant contribution of metal-rich ([Fe/H] $\gtrsim -1$) stars. This property had already been noticed by several authors (e.g., Carlin et al. 2018; Hayes et al. 2020) and is recovered despite the intentional bias of the SEGUE catalog to low-metallicity stars (note the excess at [Fe/H] $\lesssim -1$ in the black/

all-sample histogram; see Bonifacio et al. 2021 and Whitten et al. 2021 for discussions).

The final median [Fe/H] values we obtained for the leading and trailing arms are $-1.46^{+0.02}_{-0.03}$ and $-1.28^{+0.03}_{-0.05}$, respectively, where upper and lower limits represent bootstrapped (10^4 times) 95% confidence intervals. These metallicity values derived from SEGUE are ∼0.3–0.4 dex lower than the ones obtained from APOGEE data (Hayes et al. 2020; Limberg et al. 2022), but we recall that this is due to SEGUE's target selection function (Rockosi et al. 2022).

We further notice that the locations of these metallicity peaks for both arms of the stream are well aligned with the secondary, more metal-poor, [Fe/H] peak for stars in the core of Sgr (grayish histograms in Figure 3; Hayes et al. 2020/APOGEE[17] and Minelli et al. 2023). Although differences in metallicity scales might be at play, this observation could be relevant for the evolution of the Sgr system in the presence of the Milky Way and LMC.

From StarHorse's output, we should also, in principle, be able to access information regarding ages for individual stars as this parameter is a byproduct of the isochrone-fitting procedure (e.g., Edvardsson et al. 1993; Jørgensen & Lindegren 2005, and Sanders & Das 2018). However, there are some caveats in this approach. First, it becomes increasingly difficult to distinguish between isochrones of different ages toward both the cooler regions of the main sequence as well as the upper portions of the red giant branch (see Figure 2 of Souza et al. 2020 for a didactic visualization). However, it is still possible to circumvent this issue by looking at the turnoff and subgiant areas where isochrones tend to be better segregated (see discussion in Vickers et al. 2021). Second, even at these evolutionary stages, variations in ages and metallicities have similar effects on the color–magnitude diagram (e.g., Yi et al. 2001; Pietrinferni et al. 2004; Demarque et al. 2004; Pietrinferni et al. 2006, and Dotter et al. 2008). Hence, spectroscopic [Fe/H] values can be leveraged as informative priors to break this age–metallicity degeneracy. Third, distant non-giant stars are quite faint, which is the case for our Sgr stream sample. This is where SEGUE's exquisite depth, with targets as faint as $g = 19.5$, where g is SDSS broad band centered at 4800 Å (Fukugita et al. 1996), comes in handy.

In this spirit, we attempt to provide a first estimate of the typical ages for stars in the Sgr stream. Similar to recent efforts (Bonaca et al. 2020; Buder et al. 2022; Xiang & Rix 2022), we selected stars in the SEGUE/StarHorse low-metallicity sample near the turnoff and subgiant stages. For the sake of consistency, for this task, we utilized stellar parameters derived by StarHorse itself during the isochrone-fitting process as these will be directly correlated with the ages at hand. These turnoff and subgiant stars are mostly contained within $4.5 < \log g_{\rm SH} \lesssim 3.6$ and $T_{\rm eff,\ SH} \gtrsim 5250$ K, where the subscript "SH" indicates values from StarHorse instead of SSPP. A parallel paper describes in detail this (sub)sample with reliable ages (Queiroz et al. 2023). In any case, for the purpose of this work, we highlight that typical differences between SEGUE's atmospheric parameters and those obtained with StarHorse are at the level of SSPP's internal precision.

We found a total of 56 turnoff or subgiant stars in the Sgr stream (31 in the leading arm plus 25 in the trailing one) for which ages are most reliable (top right panel of Figure 3). As expected, these are quite faint ($17.5 < g < 19.5$), which reinforces the value of a deep spectroscopic survey such as SEGUE. Members of the Sgr stream (blue and red histograms representing leading and trailing arms, respectively) appear to be older (11–12 Gyr) than the bulk of our sample, which is mostly composed of thick-disk stars. It is reassuring that the age distribution for the entire SEGUE/StarHorse low-metallicity sample (black) peaks at 10–11 Gyr, which is, indeed, in agreement with ages derived from asteroseismic data for the chemically defined, i.e., high-α, thick-disk population (Silva Aguirre et al. 2018; Miglio et al. 2021). We quantify this visual interpretation with a kinematically selected thick-disk sample, following $100 < |\boldsymbol{V} - \boldsymbol{V}_{\rm circ}|/({\rm km\,s^{-1}}) < 180$ (check Venn et al. 2004; Bensby et al. 2014; Li & Zhao 2017; Posti et al. 2018; Koppelman et al. 2021), where $\boldsymbol{V} = (V_x, V_y, V_z)$ is the total velocity vector of a given star, i.e., $V = \sqrt{V_x^2 + V_y^2 + V_z^2}$. Within the SEGUE/StarHorse low-metallicity data (∼7800 stars), we found a median age of 10.6 Gyr for this population.

For the Sgr stream specifically, the bootstrapped median age for the leading arm is $11.6^{+0.4}_{-0.2}$ Gyr. For the trailing arm, we found $11.8^{+0.3}_{-0.2}$ Gyr. This translates to $11.7^{+0.3}_{-0.2}$ Gyr considering all Sgr stream stars. Of course, uncertainties for individual stars are still substantial, usually at the level of >25% (∼3 Gyr). Therefore, we hope that it will be possible to test this scenario, that the Sgr stream is dominated by stars older (by ∼1 Gyr) than those from the Galactic thick disk, with data provided by the upcoming generation of spectroscopic surveys, such as 4MOST (de Jong et al. 2019), SDSS-V (Kollmeier et al. 2017), and WEAVE (Dalton et al. 2016), and building on the statistical isochrone-fitting framework of StarHorse.

3.3. Evolution of Velocity Dispersion with Metallicity

The original motivation for us to identify Sgr stream members in the SEGUE/StarHorse catalog was to analyze the evolution of its kinematics extending deeply into the VMP regime, similar to Gibbons et al. (2017) and J20. The former was the first to propose the existence of two populations in the Sgr stream. Its main limitation was the lack of complete phase-space information, which are now available thanks to Gaia. Regarding the latter, the caveats were the small amount of (∼50) VMP stars in their sample (from the H3 survey) and potential contamination by Milky Way foreground stars (PP21). Here, instead of splitting the Sgr stream into two components, our approach is to model its velocity distribution across different [Fe/H] intervals. The results of this exercise can provide constraints to future chemodynamical simulations attempting to reproduce the Sgr system as was recently done for GSE (Amarante et al. 2022).

Figure 4 displays the distributions of total velocity (V) across different metallicity ranges, from VMP (left) to metal-rich (right). The color scheme is blue/red for the leading/trailing arm as in Figure 3. From visual inspection, one can notice that both histograms become broader at lower [Fe/H] values. In order to quantify this effect of increasing velocity dispersion (σ_V) with decreasing [Fe/H], we model these distributions, while also accounting for uncertainties, using a Markov Chain Monte Carlo (MCMC) method implemented with the emcee Python package (Foreman-Mackey et al. 2013). As in Li et al. (2017, 2018), the Gaussian log-likelihood

[17] Updated with APOGEE DR17 (Abdurro'uf et al. 2022).

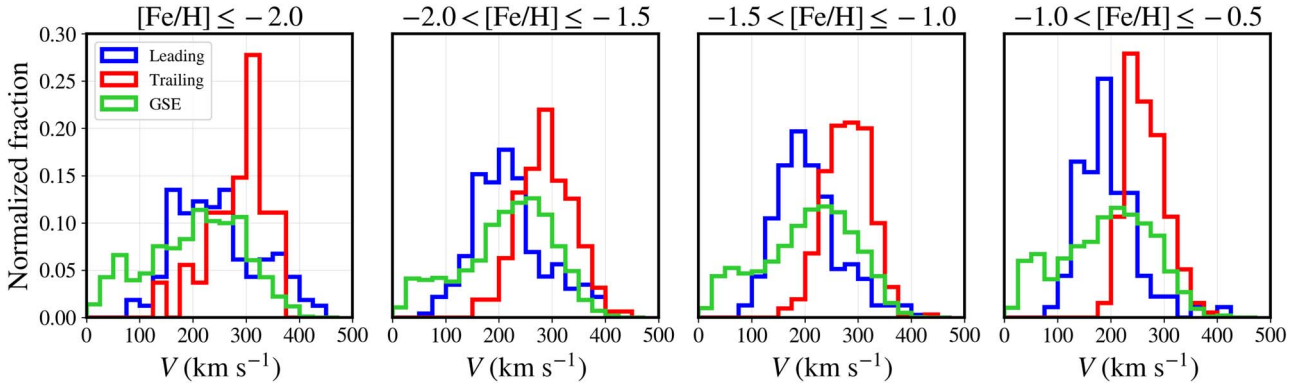

Figure 4. Distributions of $V = \sqrt{V_x^2 + V_y^2 + V_z^2}$ in intervals of [Fe/H]. From left to right, we move from the VMP to the metal-rich regime. Blue, red, and green histograms represent the leading arm, trailing arm, and GSE, respectively.

Table 1
Velocity Dispersion for the Leading and Trailing Arms of Sgr, as Well as GSE, in Bins of [Fe/H]

Substructure	σ_V (km s^{-1}) [Fe/H] $\leqslant -2.0$	σ_V (km s^{-1}) $-2.0 <$ [Fe/H] $\leqslant -1.5$	σ_V (km s^{-1}) $-1.5 <$ [Fe/H] $\leqslant -1.0$	σ_V (km s^{-1}) $-1.0 <$ [Fe/H] $\leqslant -0.5$
Leading	70^{+4}_{-4}% (194)	62^{+3}_{-3}% (284)	51^{+2}_{-2}% (405)	53^{+5}_{-4}% (94)
Trailing	44^{+6}_{-5}% (62)	38^{+3}_{-3}% (185)	32^{+2}_{-5}% (319)	28^{+2}_{-2}% (203)
GSE	87^{+2}_{-2}% (1153)	86^{+1}_{-1}% (4314)	83^{+1}_{-1}% (8020)	82^{+2}_{-2}% (1322)

function is written as

$$\log \mathcal{L} = -\frac{1}{2}\sum_{i=1}^{N}\left[\log\left(\sigma_V^2 + \sigma_{V,i}^2\right) + \frac{(V_i - \langle V\rangle)^2}{(\sigma_V^2 + \sigma_{V,i}^2)}\right], \quad (2)$$

where V_i and $\sigma_{V,i}$ are the total velocity and its respective uncertainty for the ith star within a given [Fe/H] bin. We adopt only the following uniform priors: $0 < \langle V\rangle/(\mathrm{km\,s^{-1}}) < 500$ and $\sigma_V > 0$. Lastly, we run the MCMC sampler for 500 steps with 50 walkers, including a burn-in stage of 100. Although some of the V histograms in Figure 4 show non-Gaussian tails, this exercise is sufficient for the present purpose.

The results of our MCMC calculations are presented in Table 1. Upper and lower limits are 16th and 84th percentiles, respectively, from the posterior distributions. Between $-1.5 <$ [Fe/H] $\leqslant -0.5$, we found no statistically significant ($<1\sigma$) evidence for σ_V variations. However, at [Fe/H] $\leqslant -1.5$, the σ_V increases substantially for both arms. According to present data, the VMP component of the Sgr stream (left panel of Figure 4) is dynamically hotter than its metal-rich counterpart at the $\gtrsim 2\sigma$ level. We also verified that this effect is less prominent ($\sim 1\sigma$) for GSE (green histograms in Figure 4; Table 1) even with a not-so-pure (at least 18% contamination; Limberg et al. 2022) selection (Feuillet et al. 2020), which is to be expected given the advanced stage of phase mixing of this substructure.

Now, we put our results in context with those in the literature. With the understanding that the Sgr stream is comprised of two kinematically distinct populations (V21), the increasing σ_V as a function of decreasing metallicity can be interpreted as larger fractions of the *diffuse* (J20) component contributing to the low-[Fe/H] (dynamically hotter) bins. On the contrary, the *main* component, which contains most of the stars of the substructure, is preferentially associated with the high-[Fe/H] (dynamically colder) intervals.

PP21 recently argued that the broad velocity distribution for metal-poor stars in the Sgr stream could be an artifact of Milky Way contamination in the J20 Sgr stream data. However, this effect is still clearly present in our 2× larger sample with more rigorous selection criteria. To summarize, in the low-metallicity regime, there appears to be a considerable contribution from both ancient and recently formed wraps of the stream. On the other hand, at high metallicities ([Fe/H] > -1.0), only the newest wrap is represented.

4. Model Comparisons

In this section, we interpret the phase-space properties of the Sgr stream and how they correlate with chemistry via the comparison of our Sgr sample with the V21 model.

4.1. Model Properties, Assumptions, and Limitations

V21's is a tailored N-body model of the Sgr system designed to match several properties of its tidal tails. In particular, in order to mimic the aforementioned misalignment between the stream track and its proper motions in the leading arm, the authors invoke the presence of an LMC with a total mass of $1.5 \times 10^{11}\,M_\odot$, compatible with the findings in Erkal et al. (2019), Shipp et al. (2021), and Koposov et al. (2022). The initial conditions are set to reproduce the present-day positions and velocities of both Sgr and LMC building on earlier results (Vasiliev & Belokurov 2020). However, unlike the LMC and Sgr, the Milky Way is not modeled in a live N-body scheme. Hence, it comes with the limitation that V21 depend on the Chandrasekhar analytical prescription for dynamical friction (e.g., Mo et al. 2010). See Ramos et al. (2022) for a discussion on how this approximation might influence the stripping history of the stream.

In the fiducial model, the initial stellar mass of the Sgr dSph is $2 \times 10^8\,M_\odot$ and follows a spherical King density profile (King 1962). Moreover, the system is embedded in an,

also spherical, extended dark matter halo of $3.6 \times 10^9\, M_\odot$. Other key features of V21's work is the capability of recovering crucial kinematic and structural features of Sgr's remnant (as in Vasiliev & Belokurov 2020), accounting for perturbations introduced by the gravitational field of the LMC (Garavito-Camargo et al. 2019; Cunningham et al. 2020; Petersen & Penarrubia 2020; Erkal et al. 2021; Garavito-Camargo et al. 2021; Petersen & Penarrubia 2021), and properly following mass loss suffered by the system.

Despite the close match between observations and the V21 model, there are a few limitations that could affect their results. For instance, the model does not account for the gaseous component, which may be relevant for the distribution of the debris as discussed in Wang et al. (2022) and references therein. An additional caveat is the lack of bifurcations in the modeled stream, as originally observed by Belokurov et al. (2006) and Koposov et al. (2012, see discussions by Oria et al. 2022). Finally, Sgr likely experienced at least one pericentric passage $\gtrsim$6 Gyr ago as can be inferred from dynamical perturbations in the Galactic disk (Binney & Schonrich 2018; Laporte et al. 2018, 2019; Bland-Hawthorn & Tepper-Garcia 2021; McMillan et al. 2022, and see Antoja et al. 2018) as well as the star formation histories of both the Milky Way (Ruiz-Lara et al. 2020) and Sgr itself (Siegel et al. 2007; de Boer et al. 2015). Hence, the V21 simulation, which starts only 3 Gyr in the past, is unable to cover this earlier interaction.

4.2. New and Old Wraps

Figure 5 shows observational and simulation data in ($\Lambda_{\rm Sgr}$, $v_{\rm los}$), where $\Lambda_{\rm Sgr}$ is the stream longitude coordinate as defined by Majewski et al. (2003) based on Sgr's orbital plane. Leading/trailing arm stars are represented by blue/red dots. These are overlaid on the V21 model, where gray and colored points denote dark matter and stellar particles, respectively. We split these simulated particles according to their stripping time ($t_{\rm strip}$[18]). For the remainder of this paper, we refer to the portion of the (simulated) stream formed more recently ($t_{\rm strip} < 2$ Gyr) as the *new* wrap (green). The more ancient ($t_{\rm strip} > 2$ Gyr) component is henceforth the *old* wrap (orange). Stellar particles that are still bound to the progenitor by the end of the simulation (redshift $z = 0$) are colored black.

We divide our Sgr stream data into the same metallicity intervals as in Figure 4 and Table 1. Essentially, our selected members of the Sgr stream share all regions of phase space with the V21 model particles. Notwithstanding, the bottom-most panel of Figure 5 reveals a first interesting feature. Metal-rich stars in the sample are almost exclusively associated with the new wrap, though this is more difficult to immediately assert for the leading arm because of the overlap between new and old portions within $180^\circ \lesssim \Lambda_{\rm Sgr} < 300^\circ$.

As we move toward the lower metallicity (upper) panels of Figure 5, we see larger fractions of observed Sgr stream stars coinciding with the old wrap in phase space. At the same time, the dense groups of stars overlapping with the new wrap fade away as we reach the VMP regime (top panel). As a direct consequence, stream members are more spread along the $v_{\rm los}$ axis in Figure 5, which, then, translates into the higher σ_V discussed in Section 3.3 for metal-poor/VMP stars. In general, the new wrap is preferentially associated with metal-rich stars, but also extends into the VMP realm. Conversely, the old component contains exclusively metal-poor ([Fe/H] $\lesssim -1$) stars. Therefore, these suggest that, at low metallicities, the Sgr stream is composed of a mixture between old and new wraps and this phenomenon drives the increasing σ_V quantified in Table 1.

4.3. Sgr dSph Before its Disruption

The dichotomy between metal-rich/cold and metal-poor/hot portions of the Sgr stream has been suggested, by J20, to be linked to the existence of a stellar halo-like structure in the Sgr dSph prior to its infall. This stellar halo would have larger velocity dispersion, be spatially more extended, and have lower metallicity than the rest of the Sgr galaxy. As a consequence of its kinematics, this component would be stripped at earlier times. Indeed, we verified that the old wrap of the Sgr stream stripped >2 Gyr ago in V21's model, is mainly associated with metal-poor stars (Figure 5), in conformity with J20's hypothesis. Meanwhile, the majority of the most metal-rich stars can be attributed to the new wrap. In order to check how the present-day properties of the Sgr stream are connected to those of its dSph progenitor, hence testing other conjectures of J20, we now look at the initial snapshot of V21's simulation, including the satellite's orbit and disruption history.

Simply to comprehend the assembly of the stream over time according to the V21 model, we plot the distribution of $t_{\rm strip}$ in the left panel of Figure 6. The excess at $t_{\rm strip} = 0$ is due to N-body particles that remain bound to the progenitor. On top of these histograms, we add the trajectory of the Sgr dSph in the simulation (blue line and dots) in terms of its Galactocentric distance. With this visualization, it is clear how intense episodes of material being stripped (at both $2.0 < t_{\rm strip}/{\rm Gyr} \lesssim 2.7$ and $0.5 \lesssim t_{\rm strip}/{\rm Gyr} \lesssim 1.5$) are intrinsically related to close encounters between Sgr and the Milky Way (at ~2.5 and ~1.2 Gyr ago), which originates the new and old wraps discussed in Section 4.2. Also, note how most of the material is associated with the recently formed component (new wrap) of the stream.

In order to test J20's conjecture that the stripped portion of the Sgr dSph associated with the formation of the old wrap was already dynamically hotter than the new one prior to the galaxy's disruption, we check the σ_V, with respect to Sgr, of these components in the initial snapshot of V21's simulation, which starts 3 Gyr in the past (redshift $z \sim 0.25$ in Planck Collaboration et al. 2020 cosmology). Indeed, the σ_V of stars that end up forming the old wrap, i.e., stripped at earlier times, is higher (~18 km s^{-1}) in comparison to the σ_V of stars from the new component (~14 km s^{-1}).

In the middle panel of Figure 6, the initial snapshot is presented in configuration space as $(X, Y)_{\rm Sgr,0}$, an Sgr-centered frame. The orange dots ($t_{\rm strip} > 2$ Gyr/old wrap) in this plot are less centrally concentrated (90% of stellar particles within ~4 kpc) than the green ones ($t_{\rm strip} < 2$ Gyr/new wrap; 90% within 3 kpc). This behavior is clear from the right panel of the same figure that shows the cumulative distributions of galactocentric radii ($r_{\rm Sgr,0}$) in the same system. Also, stars that remain bound until redshift $z = 0$ have even lower σ_V (~11 km s^{-1}) and are spatially more concentrated (90% within < 2 kpc) than the other components.

From the above-described properties of the V21 model, we can infer that the periphery of the simulated Sgr dSph contains a larger fraction of stars that end up as the old wrap (stripped earlier) in comparison to its central regions. Therefore, with the understanding that the old wrap is essentially composed of low-

[18] Formally, $t_{\rm strip}$ is defined as the most recent time when a particle left a 5 kpc radius sphere around the progenitor as discussed in V21.

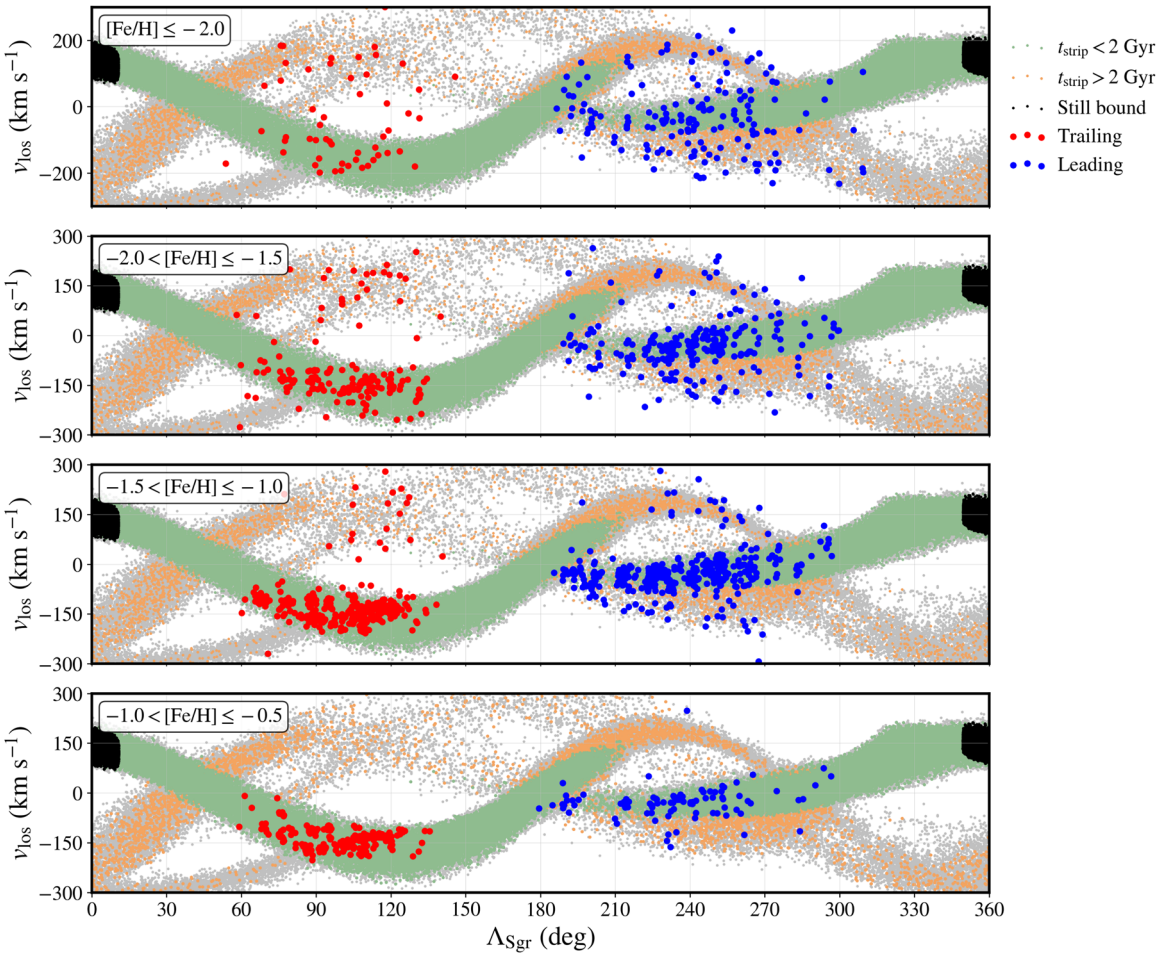

Figure 5. The Sgr stream in (Λ_{Sgr}, v_{los}) space. As in Figure 3, blue and red dots denote stars associated with the leading and trailing arms, respectively. Dark matter and stellar particles from the V21 model are shown as gray and colored dots, respectively. Green dots are attributed to the new ($t_{strip} < 2$ Gyr) and orange ones to the old ($t_{strip} > 2$ Gyr) wraps. Black dots remain bound to the progenitor until the present day (redshift $z = 0$), i.e., the end of the simulation. From top to bottom, we move from the VMP to the metal-rich regime following the same [Fe/H] ranges of Figure 4 and Table 1.

metallicity stars), we reach the conclusion that the core regions of the Sgr dSph were more metal-rich than its outskirts prior to its accretion. We recall that, indeed, previous works reported evidence for a metallicity gradient in the Sgr remnant (Bellazzini et al. 1999; Layden & Sarajedini 2000; Siegel et al. 2007; McDonald et al. 2013; Mucciarelli et al. 2017; Vitali et al. 2022). Nevertheless, fully understanding how these stellar-population variations in the Sgr system relate to its interaction with the Milky Way remains to be seen (for example, via induced star formation bursts; Hasselquist et al. 2021).

Although our interpretation favors a scenario where the Sgr dSph had enough time to develop a metallicity gradient before its disruption, quantifying this effect is difficult. One way to approach this would be by *painting* the model with ad hoc metallicity gradients, and, then comparing with, for instance, the present-day [Fe/H] variations observed across the Sgr stream (Hayes et al. 2020 and references therein). We defer this exploration to a forthcoming paper.

5. Chemical Abundances

5.1. α Elements

Apart from T_{eff}, $\log g$, and [Fe/H], the SSPP also estimates α-element abundances based on the wavelength range of $4500 \leqslant \lambda/\text{Å} \leqslant 5500$ (Lee et al. 2011), which contains several Ti I and Ti II lines as well as the Mg I triplet (∼5200 Å). de Boer et al. (2014) utilized [α/Fe] values made available by SEGUE for stars in the Sgr stream to argue that a *knee* existed at [Fe/H] $\lesssim -1.3$ in the [α/Fe]–[Fe/H] diagram (Wallerstein 1962; Tinsley 1979) for this substructure. However, this result is not supported by contemporaneous high-resolution spectroscopic data, especially from APOGEE (Hayes et al. 2020; Limberg et al. 2022; Horta et al. 2023), also H3 (Johnson et al. 2020; Naidu et al. 2020). If the position of Sgr's α knee was truly located at such high [Fe/H], it would imply that it should be even more massive than GSE under standard chemical-evolution prescriptions (e.g., Matteucci & Brocato 1990).

Here, we revisit the α abundances for the Sgr stream using SEGUE, but with a larger sample with lower contamination. In the left panel of Figure 7, we can see the continuous decrease of [α/Fe] as a function of increasing metallicity for both the Sgr stream and GSE. Most important, at a given value of [Fe/H], the median [α/Fe] of the Sgr stream (both leading and trailing arms) is lower than GSE's. This difference becomes more prominent at [Fe/H] $\gtrsim -1.5$, in agreement with the aforementioned high-resolution spectroscopy results from both H3 and APOGEE. Despite that, the low accuracy/precision of [α/Fe]

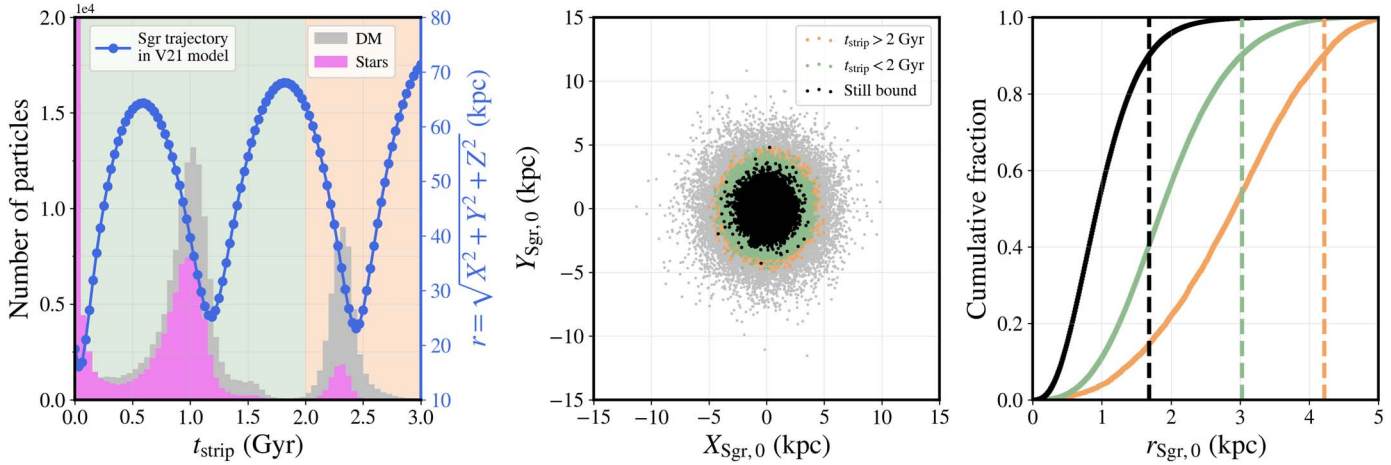

Figure 6. Left: distributions of $t_{\rm strip}$ for dark matter (gray) and stellar (pink) particles in the V21 model of the Sgr (stream+dSph) system. The orbital trajectory of Sgr in the form of Galactocentric distance is presented as the overlapping blue line and circles. Middle: dark matter and stellar (colored dots) particles in configuration space, where $(X, Y)_{\rm Sgr,0}$ denote spatial coordinates in an Sgr-centered system in the initial snapshot of the same V21 model (see the text). Right: cumulative distribution functions of galactocentric radii ($r_{\rm Sgr,0}$) of the same model particles, also centered around Sgr in the initial snapshot. Vertical dashed lines mark the positions containing 90% of the stars of each component. In all panels, the color scheme is the same as in Figure 5, where orange represents stars that end up as the old wrap of the stream ($t_{\rm strip} > 2$ Gyr), green is for the new wrap ($t_{\rm strip} < 2$ Gyr), and black are those particles that remain bound to the Sgr dSph until present-day/end of the simulation ($t_{\rm strip} = 0$).

in SEGUE still makes it difficult to attribute stars to certain populations on an individual basis.

5.2. Carbon

With the SEGUE low-metallicity data at hand, we also explore carbon abundances. In particular, we are interested in finding carbon-enhanced metal-poor (CEMP; $[{\rm C/Fe}] > +0.7$ and $[{\rm Fe/H}] < -1$; see Beers & Christlieb 2005; Aoki et al. 2007, and Placco et al. 2014) stars in the Sgr stream. The reasoning for that being the recent results by Chiti et al. (2020), and also Hansen et al. (2018) and Chiti & Frebel (2019), where these authors found no CEMP star in their sample of Sgr dSph members within $-3.1 < [{\rm Fe/H}] \lesssim -1.5$. Moreover, we utilize observations of the Sgr stream as a shortcut to check for potential differences in CEMP fractions between a dwarf galaxy and the Milky Way's stellar halo (see Venn et al. 2012; Kirby et al. 2015; Salvadori et al. 2015; Chiti et al. 2018) in a homogeneous setting. Given that the CEMP phenomenon, especially at $[{\rm Fe/H}] \lesssim -2.5$, is connected to nucleosynthesis events associated with the first generations of stars, perhaps Population III (e.g., Nomoto et al. 2013; Yoon et al. 2016; Chiaki et al. 2017), identifying such objects provide clues about the first chemical-enrichment processes that happened in a galaxy.

Throughout this section, we consider carbon abundances obtained for SEGUE spectra by (Lee et al. 2013, see also Carollo et al. 2012; Lee et al. 2017, 2019, and Arentsen et al. 2022). Inconveniently, this catalog also comes with slight variations of the stellar atmospheric parameters in comparison with the public SEGUE DR9 release. Therefore, in order to confidently identify CEMP stars, we first select candidates using only Lee et al. (2013) [C/Fe] and [Fe/H] (subscripts "L13" in Figure 7). Then, we compare $[{\rm Fe/H}]_{\rm L13}$ with [Fe/H] values from our standard DR9 sample ($[{\rm Fe/H}]_{\rm DR9}$ (the right panel of Figure 7) to confirm their low-metallicity nature.

The middle panel of Figure 7 ([C/Fe]–[Fe/H]) exhibits our selection of CEMP candidates (yellow box). Note that we take only those stars at $[{\rm Fe/H}]_{\rm L13} < -1.5$, for consistency with the metallicity range covered by Chiti et al. (2020). Expanding this boundary to $[{\rm Fe/H}]_{\rm L13} < -1$ would only include a couple of additional CEMP candidates. We discovered a total of 39 likely CEMP stars (33 at $[{\rm Fe/H}]_{\rm L13} < -2$). With this sample at hand, we looked for those candidates confidently (3σ in $[{\rm C/Fe}]_{\rm L13}$) encompassed by the CEMP criteria. We found seven such objects, shown as star symbols in Figure 7. Although two of these CEMP stars have discrepant metallicity determinations ($[{\rm Fe/H}]_{\rm L13}$ versus $[{\rm Fe/H}]_{\rm DR9}$ (the right panel of Figure 7), we can still confidently assert that there exist CEMP stars in the Sgr stream.

A possible explanation for the lack of CEMP stars in Chiti et al. (2020)'s sample could be their photometric target selection, which was based on SkyMapper DR1 (Wolf et al. 2018). The excess of carbon, hence the exquisite strength of the CH *G* band, is capable of depressing the continuum extending to the wavelength region of the Ca II K/H lines, close to the center of SkyMapper's *v* filter (3825 Å; see Da Costa et al. 2019 and references therein), a phenomenon referred to as *carbon veiling* (Yoon et al. 2020). A scenario where, if confirmed, the surviving core of the Sgr dSph has a lower CEMP fraction than its outskirts/stream at a given metallicity could be similar to what potentially happens to the Milky Way's bulge and halo (Arentsen et al. 2021). Either way, the unbiased discovery of additional VMP stars in Sgr as well as other dSph satellites (e.g., Skúladóttir et al. 2021) will be paramount for us to advance our understanding of the earliest stages of chemical enrichment in these systems.

Finally, we also calculate the fraction of CEMP stars in the Sgr stream and compare it with the Milky Way. Arentsen et al. (2022) have recently demonstrated that various observational efforts focused on the discovery and analysis of metal-poor stars via low/medium-resolution (up to $\mathcal{R} \sim 3000$) spectroscopy report inconsistent CEMP fractions among them (Lee et al. 2013; Placco et al. 2018; Aguado et al. 2019; Placco et al. 2019; Yuan et al. 2020b; Arentsen et al. 2020; Limberg et al. 2021a; Shank et al. 2022). However, we reinforce that it is not our goal to provide absolute CEMP fractions (e.g., Rossi et al. 2005; Lucatello et al. 2006; Yoon et al. 2018), but rather use the SEGUE/`StarHorse` low-metallicity sample to make a homogeneous comparison. For this

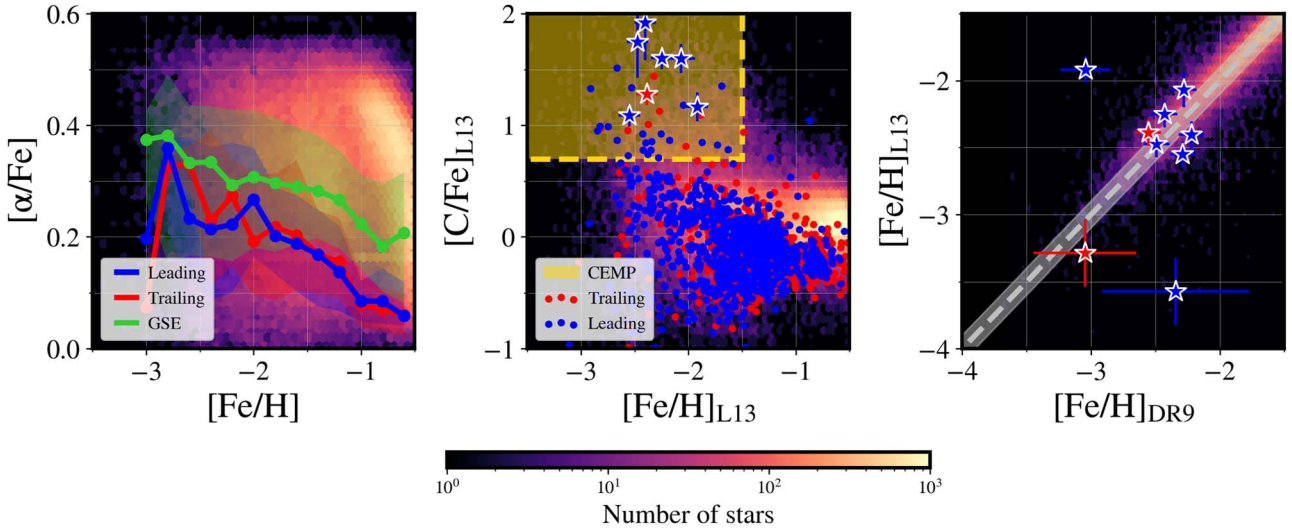

Figure 7. Left: [α/Fe]–[Fe/H]. The green line denotes the running median of GSE's [α/Fe] values in bins of 0.2 dex in [Fe/H], with the shaded area covering the 16th and 84th percentiles. Blue and red lines and shaded regions are the same, but for the leading and trailing arms of the Sgr stream, respectively. Middle: [C/Fe]–[Fe/H]. The yellow rectangle marks the locus of CEMP stars. Blue/red symbols represent leading/trailing arm stars. Candidate (3σ; see the text) CEMP stars are shown as star symbols. Right: $[Fe/H]_{L13}$–$[Fe/H]_{DR9}$, where the "L13"and "DR9" subscripts refer to [Fe/H] values either from Lee et al. (2013) or SEGUE's standard catalog from SDSS DR9. Background density maps represent the full SEGUE/`StarHorse` low-metallicity sample.

reason, we do not perform any evolutionary corrections (as in Placco et al. 2014) to the carbon abundances of Lee et al. (2013). The overall fraction of CEMP stars in the whole sample at [Fe/H] < -2, but excluding Sgr, is $19\% \pm 1\%$[19] within the same $\log g$ range. For the whole Sgr stream, leading and trailing arms altogether, this number is $16\% \pm 5\%$. Limiting our analysis to only giants ($T_{\rm eff} < 5800$ K and $\log g < 4$), we find 12% for both the stream and full sample. Therefore, we conclude the SEGUE carbon-abundance data does not provide evidence for variations in the CEMP frequency between Sgr (stream) and the Milky Way.

6. Conclusions

In this work, we performed a chemodynamical study of the Sgr stream, the tidal tails produced by the ongoing disruption of the Sgr dSph galaxy. Because of recent literature results, we were particularly interested in exploring the VMP regime of this substructure. Our main goals were to quantify the kinematic properties of this population as well as search for CEMP stars. For the task, we leveraged low-resolution spectroscopic and astrometric data from SEGUE DR9 and Gaia EDR3, respectively. Moreover, this catalog was combined with broadband photometry from various sources in order to deliver precise distances for ~175,000 low-metallicity ([Fe/H] $\leqslant -0.5$) stars via Bayesian isochrone fitting in a new `StarHorse` run (Figure 1), an effort that is fully described in an accompanying paper (Queiroz et al. 2023). Our main conclusions can be summarized as follows.

1. We delineated a new set of selection criteria for the Sgr stream based on angular momenta and actions (Figure 2). Despite being more conservative than previous works (e.g., J20 and Naidu et al. 2020), we identify ~1600 members of the Sgr stream, which is twice as many as these authors. Out of these, there are >200 VMP stars as well as seven GCs.
2. Reassuringly, although the SEGUE target selection inflates the number of metal-poor stars ([Fe/H] < -1; Figure 3), we found the leading arm to be more metal-poor, by ~0.2 dex, than the trailing one. This is in agreement with many previous works (notably Hayes et al. 2020).
3. We provided the first age estimates for individual stars in the Sgr stream. For the task, we constructed a subsample of 56 turnoff/subgiant stars in this substructure, for which `StarHorse` ages are most reliable. We found an overall median age of $11.7^{+0.3}_{-0.2}$ Gyr, which is ~1 Gyr older than the bulk of thick-disk stars according to both our own SEGUE/`StarHorse` data as well as asteroseismic estimates (Miglio et al. 2021).
4. We found (2σ) evidence for increasing velocity dispersion in the Sgr stream between its metal-rich and VMP populations (Figure 4 and Table 1). Similar findings were presented by J20, but were contested by PP21. Now, we reassert the former's findings with a 2× larger sample and more rigorously selected Sgr stream members.
5. With the *N*-body model of J20, we found that the new wrap (composed of stars recently stripped; $t_{\rm strip} < 2$ Gyr) of the Sgr stream preferentially contains metal-rich ([Fe/H] > -1.0) stars. Conversely, the old wrap ($t_{\rm strip} > 2$ Gyr) is exclusively associated with metal-poor stars ([Fe/H] < -1.0) in phase space. Hence, the increasing velocity dispersion with decreasing [Fe/H] is driven by the mixture between these components, i.e., larger fractions of the old wrap are found at lower metallicities, while the metal-rich population is only representative of the new wrap (Figure 5).
6. Looking at the initial snapshot of the J20 simulation, we found that stars that end up forming the old wrap are dynamically hotter and less centrally concentrated than those that compose the new wrap. With the understanding that the old wrap contains stars of lower metallicities, this implies that the outskirts of the Sgr dSph, prior to disruption, were more metal-poor than its core regions, i.e., internal [Fe/H] variations in the galaxy.

[19] Uncertainties for fractions are given by Wilson score confidence intervals (Wilson 1927). See Limberg et al. (2021a) for details.

7. On the chemical-abundance front, SEGUE data allowed us to verify that the [α/Fe] of the Sgr stream decreases with increasing [Fe/H]. Most important, at a given metallicity, we ascertained that the median [α/Fe] of the Sgr stream is lower than GSE's, in conformity with other recent efforts (Hasselquist et al. 2021; Limberg et al. 2022; Horta et al. 2023).
8. We confidently ($>3\sigma$) identify CEMP stars in the Sgr stream. Also, its CEMP fraction is compatible (1σ) with the overall SEGUE catalog. Hence, we argue that the apparent lack of CEMP stars in the Sgr dSph (Chiti et al. 2020, and references therein) could be associated with target selection effects and/or small sample sizes.

This paper emphasizes how powerful the synergy between deep spectroscopy and astrometric data can be in our quest to unravel the outer Galactic halo. It also shows how crucial the fully Bayesian approach of `StarHorse` is for the task of deriving precise parameters (mainly distances) even for faint stars. In fact, the SEGUE/`StarHorse` catalog provides a glimpse of the scientific potential that will be unlocked by the next generation of wide-field surveys such as 4MOST, SDSS-V, and WEAVE. Finally, we reinforce the importance of tailored *N*-body models as fundamental tools for interpreting the complex debris left behind by disrupted dwarf galaxies in the Milky Way's halo.

The authors thank the referee of this paper for a timely and constructive review that has contributed to this work. G.L. is indebted to Alex Ji, Ani Chiti, Felipe Almeida-Fernandes, Ting Li, and Vini Placco for discussions and suggestions that contributed to the original manuscript as well as Anke Arentsen who provided feedback on a preprint version of it. G.L. also thanks several authors who provided observational or simulation data, namely, Alice Minelli, Amina Helmi, Emma Dodd, Khyati Malhan, Sergey Koposov, and Zhen Yuan. G.L. is particularly grateful to Eugene Vasiliev, who readily provided the initial snapshot of the V21 simulation as well as assistance with the model. Finally, G.L. thanks all those authors who made their observational and/or simulation data publicly available and are referenced throughout this work. G.L., H.D.P., S.R., J.A., and R.M.S. extend heartfelt thanks to all involved with the "Brazilian Milky Way group meeting," namely, Eduardo Machado-Pereira, Fabrícia O. Barbosa, Hélio J. Rocha-Pinto, Lais Borbolato, Leandro Beraldo e Silva, and Yuri Abuchaim.

G.L. acknowledges FAPESP (procs. 2021/10429-0 and 2022/07301-5). H.D.P. also thanks FAPESP (procs. 2018/21250-9 and 2022/04079-0). S.R. thanks support from FAPESP (procs. 2014/18100-4 and 2015/50374-0), CAPES, and CNPq. J.A. acknowledges funding from the European Research Council (ERC) under the European Union's Horizon 2020 research and innovation program (grant agreement No. 852839). R.M.S. acknowledges CNPq (proc. 306667/2020-7). A.P.-V. acknowledges the DGAPA-PAPIIT grant IA103122. Y.S.L. acknowledges support from the National Research Foundation (NRF) of Korea grant funded by the Ministry of Science and ICT (NRF-2021R1A2C1008679). Y.S.L. also gratefully acknowledges partial support for his visit to the University of Notre Dame from OISE-1927130: The International Research Network for Nuclear Astrophysics (IReNA), awarded by the US National Science Foundation.

This work has made use of data from the European Space Agency (ESA) mission Gaia (https://www.cosmos.esa.int/gaia), processed by the Gaia Data Processing and Analysis Consortium (DPAC, https://www.cosmos.esa.int/web/gaia/dpac/consortium). Funding for the DPAC has been provided by national institutions, in particular, the institutions participating in the Gaia Multilateral Agreement.

Funding for the Sloan Digital Sky Survey IV has been provided by the Alfred P. Sloan Foundation, the U.S. Department of Energy Office of Science, and the Participating Institutions. SDSS-IV acknowledges support and resources from the Center for High Performance Computing at the University of Utah. The SDSS website is www.sdss.org. SDSS-IV is managed by the Astrophysical Research Consortium for the Participating Institutions of the SDSS Collaboration.

This research has made use of the VizieR catalog access tool, CDS, Strasbourg, France (https://cds.u-strasbg.fr). The original description of the VizieR service was published in Ochsenbein et al. (2000).

Software: `corner` (Foreman-Mackey 2016), `gala` (Price-Whelan 2017), `jupyter` (Kluyver et al. 2016), `matplotlib` (Hunter 2007), `NumPy` (van der Walt et al. 2011), `pandas` (The pandas development team 2020), `SciPy` (Virtanen et al. 2020), `scikit-learn` (Pedregosa et al. 2012), `TOPCAT` (Taylor 2005).

Appendix
Other Dwarf-galaxy Polar Streams

In order to test if our Sgr stream selection is robust against the presence of other known dwarf-galaxy polar stellar streams (see Malhan et al. 2021), we assembled literature data for Cetus (Yuan et al. 2019, originally found by Newberg et al. 2009), Orphan (Koposov et al. 2019, first described by Belokurov et al. 2006, 2007), LMS-1/Wukong (Yuan et al. 2020a, also Naidu et al. 2020), and the Helmi streams (O'Hare et al. 2020, discovered by Helmi et al. 1999). In this process, we made an effort to compile only members of streams found with automatic algorithms (Myeong et al. 2018a, 2018b; Yuan et al. 2018). The only exception is Orphan, whose members were selected based on the stream's track on the sky as well as proper motions. Note that, originally, Yuan et al. (2020a) dubbed the LMS-1/Wukong substructure as a *low-mass stellar-debris stream*, hence the acronym. Almost at the same time, Naidu et al. (2020) identified a very similar dynamical group of stars in (L_z, E) with the H3 survey and referred to it as "Wukong." For now, we keep both nomenclatures, similar to what several authors adopt for GSE. Apart from the $J_z > J_R$ condition, we followed Naidu et al. (2022) and (Limberg et al. (2021b), which builds on the works of Koppelman et al. (2019), Aguado et al. (2021), and Limberg et al. (2021c) to apply further constraints to both Orphan and the Helmi streams, respectively, in order to guarantee better purity for these samples.

The kinematic/dynamical locus occupied by the polar streams is shown in Figure 8. Crucially, they do not overlap the box in (L_z, L_y) defined for Sgr (the yellow region in the left panel). However, note how the J20 criteria actually encompass the bulk of Orphan stream stars, which emphasizes the importance of our more rigorous selection. Helmi stream stars are the ones that reach the closest to our Sgr boundary in angular-momentum space. Although no stars from this

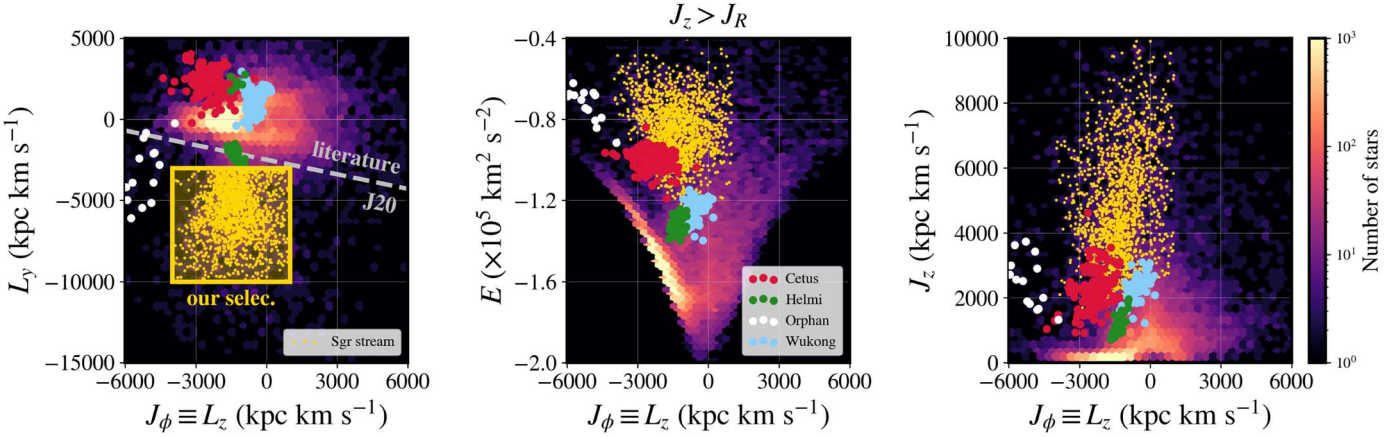

Figure 8. Similar to the top row of Figure 2 ($J_z > J_R$), but including literature data for dwarf-galaxy polar streams. Left: (L_z, L_y). The dashed line shows the J20 criterion for selecting Sgr members. The yellow box exhibits our criteria. Colored dots represent stars from Sgr (yellow), Cetus (red), Orphan (white), LMS-1/Wukong (blue), and Helmi (green) streams (see text). Middle: (L_z, E). Right: (L_z, J_z) In all panels, density maps represent the full SEGUE/`StarHorse` low-metallicity sample.

substructure actually fulfill our entire set of selection criteria for Sgr, it is difficult to assert that Helmi stream interlopers are nonexistent in our Sgr sample. One way to quantify the cross-contamination between halo substructures would be to explore *N*-body models, similar to what has been recently done by Sharpe et al. (2022). For the time being, even without such a dedicated effort, we highlight that our criteria achieve several benchmarks, such as eliminating >90% of potential GSE stars, removing low-J_z contaminants from the Galactic disk(s), and excluding most stars from other well-known dwarf-galaxy streams.

ORCID iDs

Guilherme Limberg https://orcid.org/0000-0002-9269-8287
Anna B. A. Queiroz https://orcid.org/0000-0001-9209-7599
Hélio D. Perottoni https://orcid.org/0000-0002-0537-4146
Silvia Rossi https://orcid.org/0000-0001-7479-5756
João A. S. Amarante https://orcid.org/0000-0002-7662-5475
Rafael M. Santucci https://orcid.org/0000-0002-7529-1442
Cristina Chiappini https://orcid.org/0000-0003-1269-7282
Angeles Pérez-Villegas https://orcid.org/0000-0002-5974-3998
Young Sun Lee https://orcid.org/0000-0001-5297-4518

References

Abdurro'uf, Accetta, K., Aerts, C., et al. 2022, ApJS, 259, 35
Aguado, D. S., Youakim, K., Gonzalez Hernandez, J. I., et al. 2019, MNRAS, 490, 2241
Aguado, D. S., Myeong, G. C., Belokurov, V., et al. 2021, MNRAS, 500, 889
Ahn, C. P., Alexandroff, R., Allende Prieto, C., et al. 2012, ApJS, 203, 21
Alard, C. 1996, ApJL, 458, L17
Allende Prieto, C., Sivarani, T., Beers, T. C., et al. 2008, AJ, 136, 2070
Amarante, J. A. S., Debattista, V. P., Beraldo E Silva, L., Laporte, C. F. P., & Deg, N. 2022, ApJ, 937, 12
Anders, F., Khalatyan, A., Chiappini, C., et al. 2019, A&A, 628, A94
Anders, F., Khalatyan, A., Queiroz, A. B. A., et al. 2022, A&A, 658, A91
Antoja, T., Ramos, P., Mateu, C., et al. 2020, A&A, 635, L3
Antoja, T., Helmi, A., Romero-Gomez, M., et al. 2018, Natur, 561, 360
Aoki, W., Beers, T. C., Christlieb, N., et al. 2007, ApJ, 655, 492
Arentsen, A., Placco, V. M., Lee, Y. S., et al. 2022, MNRAS, 515, 4082
Arentsen, A., Starkenburg, E., Aguado, D. S., et al. 2021, MNRAS, 505, 1239
Arentsen, A., Starkenburg, E., Martin, N. F., et al. 2020, MNRAS, 496, 4964
Astropy Collaboration, Price-Whelan, A. M., Sipőcz, B. M., et al. 2018, AJ, 156, 123
Astropy Collaboration, Robitaille, T. P., Tollerud, E. J., et al. 2013, A&A, 558, A33
Beers, T. C., & Christlieb, N. 2005, ARA&A, 43, 531
Bellazzini, M., Ibata, R., Malhan, K., et al. 2020, A&A, 636, A107
Bellazzini, M., Ferraro, F. R., & Buonanno, R. 1999, MNRAS, 304, 633
Bellazzini, M., Ibata, R. A., Chapman, S. C., et al. 2008, AJ, 136, 1147
Bellazzini, M., Newberg, H. J., Correnti, M., Ferraro, F. R., & Monaco, L. 2006, A&A, 457, L21
Belokurov, V., Erkal, D., Evans, N. W., Koposov, S. E., & Deason, A. J. 2018, MNRAS, 478, 611
Belokurov, V., Evans, N. W., Irwin, M. J., et al. 2007, ApJ, 658, 337
Belokurov, V., Koposov, S. E., Evans, N. W., et al. 2014, MNRAS, 437, 116
Belokurov, V., Zucker, D. B., Evans, N. W., et al. 2006, ApJL, 642, L137
Bennett, M., & Bovy, J. 2019, MNRAS, 482, 1417
Bensby, T., Feltzing, S., & Oey, M. S. 2014, A&A, 562, A71
Binney, J., & Schonrich, R. 2018, MNRAS, 481, 1501
Bland-Hawthorn, J., & Gerhard, O. 2016, ARA&A, 54, 529
Bland-Hawthorn, J., & Tepper-Garcia, T. 2021, MNRAS, 504, 3168
Bonaca, A., Conroy, C., Cargile, P. A., et al. 2020, ApJL, 897, L18
Bonifacio, P., Monaco, L., Salvadori, S., et al. 2021, A&A, 651, A79
Buder, S., Lind, K., Ness, M. K., et al. 2022, MNRAS, 510, 2407
Bullock, J. S., & Johnston, K. V. 2005, ApJ, 635, 931
Callingham, T. M., Cautun, M., Deason, A. J., et al. 2022, MNRAS, 513, 4107
Cargile, P. A., Conroy, C., Johnson, B. D., et al. 2020, ApJ, 900, 28
Carlin, J. L., Sheffield, A. A., Cunha, K., & Smith, V. V. 2018, ApJL, 859, L10
Carollo, D., Beers, T. C., Bovy, J., et al. 2012, ApJ, 744, 195
Chandra, V., Naidu, R. P., Conroy, C., et al. 2022, arXiv:2212.00806
Chiaki, G., Tominaga, N., & Nozawa, T. 2017, MNRAS, 472, L115
Chiti, A., & Frebel, A. 2019, ApJ, 875, 112
Chiti, A., Hansen, K. Y., & Frebel, A. 2020, ApJ, 901, 164
Chiti, A., Simon, J. D., Frebel, A., et al. 2018, ApJ, 856, 142
Chou, M.-Y., Cunha, K., Majewski, S. R., et al. 2010, ApJ, 708, 1290
Chou, M.-Y., Majewski, S. R., Cunha, K., et al. 2007, ApJ, 670, 346
Conroy, C., Bonaca, A., Cargile, P., et al. 2019, ApJ, 883, 107
Cooper, A. P., Cole, S., Frenk, C. S., et al. 2010, MNRAS, 406, 744
Cooper, A. P., D'Souza, R., Kauffmann, G., et al. 2013, MNRAS, 434, 3348
Coronado, J., Rix, H.-W., & Trick, W. H. 2018, MNRAS, 481, 2970
Crnojevic, D., Sand, D. J., Spekkens, K., et al. 2016, ApJ, 823, 19
Cunningham, E. C., Garavito-Camargo, N., Deason, A. J., et al. 2020, ApJ, 898, 4
Da Costa, G. S., Bessell, M. S., Mackey, A. D., et al. 2019, MNRAS, 489, 5900
Dalton, G., Trager, S., Abrams, D. C., et al. 2016, Proc. SPIE, 9908, 99081G
de Boer, T. J. L., Belokurov, V., Beers, T. C., & Lee, Y. S. 2014, MNRAS, 443, 658
de Boer, T. J. L., Belokurov, V., & Koposov, S. 2015, MNRAS, 451, 3489
de Jong, R. S., Agertz, O., Berbel, A. A., et al. 2019, Msngr, 175, 3
Demarque, P., Woo, J.-H., Kim, Y.-C., & Yi, S. K. 2004, ApJS, 155, 667
Dotter, A., Chaboyer, B., Jevremovic, D., et al. 2008, ApJS, 178, 89
Edvardsson, B., Andersen, J., Gustafsson, B., et al. 1993, A&A, 275, 101
Erkal, D., Belokurov, V., Laporte, C. F. P., et al. 2019, MNRAS, 487, 2685
Erkal, D., Deason, A. J., Belokurov, V., et al. 2021, MNRAS, 506, 2677

Fabricius, C., Luri, X., Arenou, F., et al. 2021, A&A, 649, A5
Fellhauer, M., Belokurov, V., Evans, N. W., et al. 2006, ApJ, 651, 167
Feuillet, D. K., Feltzing, S., Sahlholdt, C. L., & Casagrande, L. 2020, MNRAS, 497, 109
Forbes, D. A. 2020, MNRAS, 493, 847
Foreman-Mackey, D. 2016, JOSS, 1, 24
Foreman-Mackey, D., Hogg, D. W., Lang, D., & Goodman, J. 2013, PASP, 125, 306
Fukugita, M., Ichikawa, T., Gunn, J. E., et al. 1996, AJ, 111, 1748
Gaia Collaboration, Prusti, T., de Bruijne, J. H. J., et al. 2016a, A&A, 595, A1
Gaia Collaboration, Brown, A. G. A., Vallenari, A., et al. 2016b, A&A, 595, A2
Gaia Collaboration, Brown, A. G. A., Vallenari, A., et al. 2018, A&A, 616, A1
Gaia Collaboration, Brown, A. G. A., Vallenari, A., et al. 2021, A&A, 649, A1
Garavito-Camargo, N., Besla, G., Laporte, C. F. P., et al. 2019, ApJ, 884, 51
Garavito-Camargo, N., Besla, G., Laporte, C. F. P., et al. 2021, ApJ, 919, 109
Gibbons, S. L. J., Belokurov, V., & Evans, N. W. 2017, MNRAS, 464, 794
Hansen, C. J., El-Souri, M., Monaco, L., et al. 2018, ApJ, 855, 83
Hasselquist, S., Hayes, C. R., Lian, J., et al. 2021, ApJ, 923, 172
Hayes, C. R., Majewski, S. R., Hasselquist, S., et al. 2020, ApJ, 889, 63
Haywood, M., Di Matteo, P., Lehnert, M. D., et al. 2018, ApJ, 863, 113
Helmi, A. 2004, ApJL, 610, L97
Helmi, A. 2020, ARA&A, 58, 205
Helmi, A., Babusiaux, C., Koppelman, H. H., et al. 2018, Natur, 563, 85
Helmi, A., & White, S. D. M. 1999, MNRAS, 307, 495
Helmi, A., & White, S. D. M. 2001, MNRAS, 323, 529
Helmi, A., White, S. D. M., de Zeeuw, P. T., & Zhao, H. 1999, Natur, 402, 53
Hernitschek, N., Sesar, B., Rix, H.-W., et al. 2017, ApJ, 850, 96
Hogg, D. W., Eilers, A.-C., & Rix, H.-W. 2019, AJ, 158, 147
Horta, D., Schiavon, R. P., Mackereth, J. T., et al. 2023, MNRAS, 520, 5671
Hunter, J. D. 2007, CSE, 9, 90
Hyde, E. A., Keller, S., Zucker, D. B., et al. 2015, ApJ, 805, 189
Ibata, R., Bellazzini, M., Thomas, G., et al. 2020, ApJL, 891, L19
Ibata, R., Irwin, M., Lewis, G., Ferguson, A. M. N., & Tanvir, N. 2001a, Natur, 412, 49
Ibata, R., Irwin, M., Lewis, G. F., & Stolte, A. 2001b, ApJL, 547, L133
Ibata, R. A., Gilmore, G., & Irwin, M. J. 1994, Natur, 370, 194
Ibata, R. A., Gilmore, G., & Irwin, M. J. 1995, MNRAS, 277, 781
Johnson, B. D., Conroy, C., Naidu, R. P., et al. 2020, ApJ, 900, 103
Johnston, K. V. 1998, ApJ, 495, 297
Johnston, K. V., Law, D. R., & Majewski, S. R. 2005, ApJ, 619, 800
Jørgensen, B. R., & Lindegren, L. 2005, A&A, 436, 127
Kauffmann, G., White, S. D. M., & Guiderdoni, B. 1993, MNRAS, 264, 201
Keller, S. C., Yong, D., & Da Costa, G. S. 2010, ApJ, 720, 940
Kim, C., Lee, Y. S., Beers, T. C., & Masseron, T. 2022, JKAS, 55, 23
King, I. 1962, AJ, 67, 471
Kirby, E. N., Guo, M., Zhang, A. J., et al. 2015, ApJ, 801, 125
Kluyver, T., Ragan-Kelley, B., Pérez, F., et al. 2016, in Positioning and Power in Academic Publishing: Players, Agents and Agendas, ed. F. Loizides & B. Schmidt (Amsterdam: IOS Press), 87
Kollmeier, J. A., Zasowski, G., Rix, H.-W., et al. 2017, arXiv:1711.03234
Koo, J.-R., Sun Lee, Y., Park, H.-J., Kwang Kim, Y., & Beers, T. C. 2022, ApJ, 925, 35
Koposov, S. E., Rix, H.-W., & Hogg, D. W. 2010, ApJ, 712, 260
Koposov, S. E., Belokurov, V., Evans, N. W., et al. 2012, ApJ, 750, 80
Koposov, S. E., Belokurov, V., Li, T. S., et al. 2019, MNRAS, 485, 4726
Koposov, S. E., Erkal, D., Li, T. S., et al. 2023, MNRAS, in press (arXiv:2211.04495)
Koppelman, H. H., Hagen, J. H. J., & Helmi, A. 2021, A&A, 647, A37
Koppelman, H. H., Helmi, A., Massari, D., Roelenga, S., & Bastian, U. 2019, A&A, 625, A5
Kruijssen, J. M. D., Pfeffer, J. L., Chevance, M., et al. 2020, MNRAS, 498, 2472
Laporte, C. F. P., Johnston, K. V., Gomez, F. A., Garavito-Camargo, N., & Besla, G. 2018, MNRAS, 481, 286
Laporte, C. F. P., Minchev, I., Johnston, K. V., & Gomez, F. A. 2019, MNRAS, 485, 3134
Law, D. R., Johnston, K. V., & Majewski, S. R. 2005, ApJ, 619, 807
Law, D. R., & Majewski, S. R. 2010, ApJ, 714, 229
Layden, A. C., & Sarajedini, A. 2000, AJ, 119, 1760
Lee, Y. S., Beers, T. C., & Kim, Y. K. 2019, ApJ, 885, 102
Lee, Y. S., Beers, T. C., Kim, Y. K., et al. 2017, ApJ, 836, 91
Lee, Y. S., Beers, T. C., Sivarani, T., et al. 2008a, AJ, 136, 2022
Lee, Y. S., Beers, T. C., Sivarani, T., et al. 2008b, AJ, 136, 2050
Lee, Y. S., Beers, T. C., Prieto, C. A., et al. 2011, AJ, 141, 90
Lee, Y. S., Beers, T. C., Masseron, T., et al. 2013, AJ, 146, 132
Leung, H. W., & Bovy, J. 2019, MNRAS, 489, 2079
Li, C., & Zhao, G. 2017, ApJ, 850, 25
Li, J., Liu, C., Xue, X., et al. 2019, ApJ, 874, 138
Li, J., Smith, M. C., Zhong, J., et al. 2016, ApJ, 823, 59
Li, T. S., Simon, J. D., Drlica-Wagner, A., et al. 2017, ApJ, 838, 8
Li, T. S., Simon, J. D., Kuehn, K., et al. 2018, ApJ, 866, 22
Li, T. S., Koposov, S. E., Erkal, D., et al. 2021, ApJ, 911, 149
Limberg, G., Souza, S. O., Perez-Villegas, A., et al. 2022, ApJ, 935, 109
Limberg, G., Santucci, R. M., Rossi, S., et al. 2021a, ApJ, 913, 11
Limberg, G., Santucci, R. M., Rossi, S., et al. 2021b, ApJL, 913, L28
Limberg, G., Rossi, S., Beers, T. C., et al. 2021c, ApJ, 907, 10
Lindegren, L., Klioner, S. A., Hernández, J., et al. 2021a, A&A, 649, A2
Lindegren, L., Bastian, U., Biermann, M., et al. 2021b, A&A, 649, A4
Lucatello, S., Beers, T. C., Christlieb, N., et al. 2006, ApJL, 652, L37
Majewski, S. R., Skrutskie, M. F., Weinberg, M. D., & Ostheimer, J. C. 2003, ApJ, 599, 1082
Majewski, S. R., Kunkel, W. E., Law, D. R., et al. 2004, AJ, 128, 245
Majewski, S. R., Schiavon, R. P., Frinchaboy, P. M., et al. 2017, AJ, 154, 94
Malhan, K., Ibata, R. A., & Martin, N. F. 2018, MNRAS, 481, 3442
Malhan, K., Yuan, Z., Ibata, R. A., et al. 2021, ApJ, 920, 51
Malhan, K., Ibata, R. A., Sharma, S., et al. 2022, ApJ, 926, 107
Martinez-Delgado, D., Gomez-Flechoso, M. A., Aparicio, A., & Carrera, R. 2004, ApJ, 601, 242
Martinez-Delgado, D., Roman, J., Erkal, D., et al. 2021, MNRAS, 506, 5030
Massari, D., Koppelman, H. H., & Helmi, A. 2019, A&A, 630, L4
Mateo, M., Mirabal, N., Udalski, A., et al. 1996, ApJL, 458, L13
Mateo, M., Olszewski, E. W., & Morrison, H. L. 1998, ApJL, 508, L55
Matteucci, F., & Brocato, E. 1990, ApJ, 365, 539
McDonald, I., Zijlstra, A. A., Sloan, G. C., et al. 2013, MNRAS, 436, 413
McMillan, P. J. 2017, MNRAS, 465, 76
McMillan, P. J., Kordopatis, G., Kunder, A., et al. 2018, MNRAS, 477, 5279
McMillan, P. J., Petersson, J., Tepper-Garcia, T., et al. 2022, MNRAS, 516, 4988
Miglio, A., Chiappini, C., Mackereth, J. T., et al. 2021, A&A, 645, A85
Minelli, A., Bellazzini, M., Mucciarelli, A., et al. 2023, A&A, 669, A54
Mo, H., van den Bosch, F. C., & White, S. 2010, Galaxy Formation and Evolution (Cambridge: Cambridge Univ. Press)
Monaco, L., Bellazzini, M., Bonifacio, P., et al. 2007, A&A, 464, 201
Monaco, L., Bellazzini, M., Bonifacio, P., et al. 2005, A&A, 441, 141
Morinaga, Y., Ishiyama, T., Kirihara, T., & Kinjo, K. 2019, MNRAS, 487, 2718
Mucciarelli, A., Bellazzini, M., Ibata, R., et al. 2017, A&A, 605, A46
Myeong, G. C., Evans, N. W., Belokurov, V., Amorisco, N. C., & Koposov, S. E. 2018a, MNRAS, 475, 1537
Myeong, G. C., Evans, N. W., Belokurov, V., Sanders, J. L., & Koposov, S. E. 2018b, MNRAS, 478, 5449
Naidu, R. P., Conroy, C., Bonaca, A., et al. 2020, ApJ, 901, 48
Naidu, R. P., Conroy, C., Bonaca, A., et al. 2022, arXiv:2204.09057
Newberg, H. J., Willett, B. A., Yanny, B., & Xu, Y. 2010, ApJ, 711, 32
Newberg, H. J., Yanny, B., & Willett, B. A. 2009, ApJL, 700, L61
Newberg, H. J., Yanny, B., Grebel, E. K., et al. 2003, ApJL, 596, L191
Nomoto, K., Kobayashi, C., & Tominaga, N. 2013, ARA&A, 51, 457
Ochsenbein, F., Bauer, P., & Marcout, J. 2000, A&AS, 143, 23
O'Hare, C. A. J., Evans, N. W., McCabe, C., Myeong, G., & Belokurov, V. 2020, PhRvD, 101, 023006
Oria, P.-A., Ibata, R., Ramos, P., Famaey, B., & Errani, R. 2022, ApJL, 932, L14
Penarrubia, J., Belokurov, V., Evans, N. W., et al. 2010, MNRAS, 408, L26
Penarrubia, J., & Petersen, M. S. 2021, MNRAS, 508, L26
Pedregosa, F., Varoquaux, G., Gramfort, A., et al. 2012, arXiv:1201.0490
Perottoni, H. D., Limberg, G., Amarante, J. A. S., et al. 2022, ApJL, 936, L2
Petersen, M. S., & Penarrubia, J. 2020, MNRAS, 494, L11
Petersen, M. S., & Penarrubia, J. 2021, NatAs, 5, 251
Pietrinferni, A., Cassisi, S., Salaris, M., & Castelli, F. 2004, ApJ, 612, 168
Pietrinferni, A., Cassisi, S., Salaris, M., & Castelli, F. 2006, ApJ, 642, 797
Pillepich, A., Madau, P., & Mayer, L. 2015, ApJ, 799, 184
Placco, V. M., Frebel, A., Beers, T. C., & Stancliffe, R. J. 2014, ApJ, 797, 21
Placco, V. M., Beers, T. C., Santucci, R. M., et al. 2018, AJ, 155, 256
Placco, V. M., Santucci, R. M., Beers, T. C., et al. 2019, ApJ, 870, 122
Planck Collaboration, Aghanim, N., Akrami, Y., et al. 2020, A&A, 641, A6
Posti, L., Helmi, A., Veljanoski, J., & Breddels, M. A. 2018, A&A, 615, A70
Price-Whelan, A. M. 2017, JOSS, 2, 388
Price-Whelan, A. M., & Bonaca, A. 2018, ApJL, 863, L20
Queiroz, A. B. A., Anders, F., Chiappini, C., et al. 2020, A&A, 638, A76
Queiroz, A. B. A., Anders, F., Chiappini, C., et al. 2023, A&A, in press (arXiv:2303.09926)

Queiroz, A. B. A., Anders, F., Santiago, B. X., et al. 2018, MNRAS, 476, 2556
Ramos, P., Mateu, C., Antoja, T., et al. 2020, A&A, 638, A104
Ramos, P., Antoja, T., Yuan, Z., et al. 2022, A&A, 666, A64
Riley, A. H., & Strigari, L. E. 2020, MNRAS, 494, 983
Rockosi, C. M., Sun Lee, Y., Morrison, H. L., et al. 2022, ApJS, 259, 60
Rossi, S., Beers, T. C., Sneden, C., et al. 2005, AJ, 130, 2804
Ruiz-Lara, T., Gallart, C., Bernard, E. J., & Cassisi, S. 2020, NatAs, 4, 965
Rybizki, J., Green, G. M., Rix, H.-W., et al. 2022, MNRAS, 510, 2597
Salvadori, S., Skúladóttir, Á., & Tolstoy, E. 2015, MNRAS, 454, 1320
Sanders, J. L., & Das, P. 2018, MNRAS, 481, 4093
Santiago, B. X., Brauer, D. E., Anders, F., et al. 2016, A&A, 585, A42
Schonrich, R., Binney, J., & Dehnen, W. 2010, MNRAS, 403, 1829
Searle, L., & Zinn, R. 1978, ApJ, 225, 357
Shank, D., Beers, T. C., Placco, V. M., et al. 2022, ApJ, 926, 26
Sharpe, K., Naidu, R. P., & Conroy, C. 2022, arXiv:2211.04562
Shi, W. B., Chen, Y. Q., Carrell, K., & Zhao, G. 2012, ApJ, 751, 130
Shipp, N., Li, T. S., Pace, A. B., et al. 2019, ApJ, 885, 3
Shipp, N., Erkal, D., Drlica-Wagner, A., et al. 2021, ApJ, 923, 149
Siegel, M. H., Dotter, A., Majewski, S. R., et al. 2007, ApJL, 667, L57
Silva Aguirre, V., Bojsen-Hansen, M., Slumstrup, D., et al. 2018, MNRAS, 475, 5487
Skúladóttir, Á., Salvadori, S., Amarsi, A. M., et al. 2021, ApJL, 915, L30
Smolinski, J. P., Lee, Y. S., Beers, T. C., et al. 2011, AJ, 141, 89
Souza, S. O., Kerber, L. O., Barbuy, B., et al. 2020, ApJ, 890, 38
Springel, V., Frenk, C. S., & White, S. D. M. 2006, Natur, 440, 1137
Taylor, M. B. 2005, in ASP Conf. Ser. 347, Astronomical Data Analysis Software and Systems XIV, ed. P. Shopbell, M. Britton, & R. Ebert (San Francisco, CA: ASP), 29
The pandas development team 2020, pandas-dev/pandas: Pandas, v1.3.5, Zenodo, doi:10.5281/zenodo.3509134
Thomas, G. F., & Battaglia, G. 2022, A&A, 660, A29
Tinsley, B. M. 1979, ApJ, 229, 1046
van der Walt, S., Colbert, S. C., & Varoquaux, G. 2011, CSE, 13, 22
Vasiliev, E. 2019, MNRAS, 482, 1525
Vasiliev, E., & Baumgardt, H. 2021, MNRAS, 505, 5978
Vasiliev, E., & Belokurov, V. 2020, MNRAS, 497, 4162
Vasiliev, E., Belokurov, V., & Erkal, D. 2021, MNRAS, 501, 2279
Venn, K. A., Irwin, M., Shetrone, M. D., et al. 2004, AJ, 128, 1177
Venn, K. A., Shetrone, M. D., Irwin, M. J., et al. 2012, ApJ, 751, 102
Vickers, J. J., Shen, J., & Li, Z.-Y. 2021, ApJ, 922, 189
Virtanen, P., Gommers, R., Oliphant, T. E., et al. 2020, NatMe, 17, 261
Vitali, S., Arentsen, A., Starkenburg, E., et al. 2022, MNRAS, 517, 6121
Vivas, A. K., Zinn, R., & Gallart, C. 2005, AJ, 129, 189
Wallerstein, G. 1962, ApJS, 6, 407
Wang, H.-F., Yang, Y.-B., Hammer, F., & Wang, J.-L. 2022, arXiv:2204.08542
White, S. D. M., & Frenk, C. S. 1991, ApJ, 379, 52
Whitten, D. D., Placco, V. M., Beers, T. C., et al. 2021, ApJ, 912, 147
Wilson, E. B. 1927, JASA, 22, 209
Wolf, C., Onken, C. A., Luvaul, L. C., et al. 2018, PASA, 35, e010
Xiang, M., & Rix, H.-W. 2022, Natur, 603, 599
Yang, C., Xue, X.-X., Li, J., et al. 2019, ApJ, 886, 154
Yanny, B., Newberg, H. J., Johnson, J. A., et al. 2009a, ApJ, 700, 1282
Yanny, B., Rockosi, C., Newberg, H. J., et al. 2009b, AJ, 137, 4377
Yi, S., Demarque, P., Kim, Y.-C., et al. 2001, ApJS, 136, 417
Yoon, J., Whitten, D. D., Beers, T. C., et al. 2020, ApJ, 894, 7
Yoon, J., Beers, T. C., Placco, V. M., et al. 2016, ApJ, 833, 20
Yoon, J., Beers, T. C., Dietz, S., et al. 2018, ApJ, 861, 146
York, D. G., Adelman, J., Anderson, J. E., Jr., et al. 2000, AJ, 120, 1579
Yuan, Z., Chang, J., Banerjee, P., et al. 2018, ApJ, 863, 26
Yuan, Z., Chang, J., Beers, T. C., & Huang, Y. 2020a, ApJL, 898, L37
Yuan, Z., Smith, M. C., Xue, X.-X., et al. 2019, ApJ, 881, 164
Yuan, Z., Myeong, G. C., Beers, T. C., et al. 2020b, ApJ, 891, 39